5-2016

Investigation of ^{186}Re via radiative thermal-neutron capture on ^{185}Re

David A. Matters [*]
Air Force Institute of Technology

Andrew G. Lerch
Defense Threat Reduction Agency

A. M. Hurst
University of California - Berkeley

L. Szentmiklosi
Hungarian Academy of Sciences

J. J. Carroll
U. S. Army Research Laboratory

See next page for additional authors

Recommended Citation

Matters, D.A. et al. (2016). "Investigation of 186Re via radiative thermal-neutron capture on 185Re". Phys. Rev. C 93, 054319. https://doi.org/10.1103/PhysRevC.93.054319

Investigation of ^{186}Re via radiative thermal-neutron capture on ^{185}Re

D. A. Matters,[1,*] A. G. Lerch,[2] A. M. Hurst,[3,4] L. Szentmiklósi,[5] J. J. Carroll,[6] B. Detwiler,[7] Zs. Révay,[8] J. W. McClory,[1] S. R. McHale,[2] R. B. Firestone,[3] B. W. Sleaford,[9] M. Krtička,[10] and T. Belgya[5]

[1]*Air Force Institute of Technology, Wright-Patterson AFB, Ohio 45433, USA*
[2]*Defense Threat Reduction Agency, Fort Belvoir, Virginia 22060, USA*
[3]*Lawrence Berkeley National Laboratory, Berkeley, California 94720, USA*
[4]*Department of Nuclear Engineering, University of California, Berkeley, California 94720, USA*
[5]*Centre for Energy Research, Hungarian Academy of Sciences, H-1525 Budapest, Hungary*
[6]*U.S. Army Research Laboratory, Adelphi, Maryland 20783, USA*
[7]*Youngstown State University, Youngstown, Ohio 44555, USA*
[8]*Technische Universität München, 7 Heinz Maier-Leibnitz Zentrum (MLZ), Garching, Germany*
[9]*Lawrence Livermore National Laboratory, Livermore, California 94550, USA*
[10]*Charles University in Prague, Faculty of Mathematics and Physics, CZ-180 00 Prague, Czech Republic*

(Received 28 March 2016; published 16 May 2016)

Partial γ-ray production cross sections and the total radiative thermal-neutron capture cross section for the ^{185}Re$(n,\gamma)^{186}$Re reaction were measured using the Prompt Gamma Activation Analysis facility at the Budapest Research Reactor with an enriched ^{185}Re target. The ^{186}Re cross sections were standardized using well-known ^{35}Cl$(n,\gamma)^{36}$Cl cross sections from irradiation of a stoichiometric $^{\text{nat}}ReCl_3$ target. The resulting cross sections for transitions feeding the ^{186}Re ground state from low-lying levels below a cutoff energy of $E_c = 746$ keV were combined with a modeled probability of ground-state feeding from levels above E_c to arrive at a total cross section of $\sigma_0 = 111(6)$ b for radiative thermal-neutron capture on ^{185}Re. A comparison of modeled discrete-level populations with measured transition intensities led to proposed revisions for seven tentative spin-parity assignments in the adopted level scheme for ^{186}Re. Additionally, 102 primary γ rays were measured, including 50 previously unknown. A neutron-separation energy of $S_n = 6179.59(5)$ keV was determined from a global least-squares fit of the measured γ-ray energies to the known ^{186}Re decay scheme. The total capture cross section and separation energy results are comparable to earlier measurements of these values.

DOI: 10.1103/PhysRevC.93.054319

I. INTRODUCTION

The Evaluated Gamma-ray Activation File (EGAF) [1] is a coordinated research project of the International Atomic Energy Agency (IAEA) used in prompt gamma-ray neutron activation analysis (PGAA) for the determination of the elemental compositions of materials [2]. The data in the EGAF consist of capture γ-ray production cross sections (σ_γ) which were initially measured using natural elemental targets. Efforts are currently underway to improve the database using measurements on isotopically enriched targets, e.g., Ref. [3]. The methodology employed in this effort involves measurement of partial production cross sections for prompt neutron-capture γ rays using a guided thermal-neutron beam.

The total radiative thermal-neutron capture cross section σ_0 can be obtained by combining the experimental partial γ-ray production cross sections for direct population of the ground state ($\sigma_{\gamma 0}$) from low-lying levels with statistical modeling of the decay scheme to estimate the contribution of γ rays for ground-state feeding from the quasicontinuum. This method has been employed successfully with the stable palladium [4], potassium [5], gadolinium [6], and tungsten [3,7] isotopes. Recent efforts have been focused on the actinides [8,9].

The isotope ^{186}Re (half-life $T_{1/2} = 3.7186$ d [10]) has medical applications as a high specific-activity β^- emitter for the palliative treatment of bone metastases resulting from prostate and breast cancers [11]. For this purpose, ^{186}Re is generally produced by thermal-neutron capture on enriched ^{185}Re at reactors [12]. Medical isotope production activities involving neutron capture rely on accurate partial γ-ray production cross sections in order to calculate heating in the target and host vessel due to the local absorption of capture γ rays [13]. Independent measurements of total radiative thermal-neutron capture cross sections also add to the accuracy of existing evaluated data, used to plan the production of isotopes for patient treatment.

The object of this work is to further the effort of completing an in-depth spectroscopic study of ^{186}Re, for which the adopted level scheme data [10] in the Evaluated Nuclear Structure Data File (ENSDF) [14] includes numerous tentative spin-parity assignments and approximate level energies. Measured partial γ-ray cross sections from radiative thermal-neutron capture on an enriched ^{185}Re target, combined with statistical modeling of γ-ray cascades following neutron capture, provided an independent measurement of the total radiative thermal-neutron capture cross section for the ^{185}Re(n,γ) reaction. An independent determination of the neutron-separation energy S_n was also obtained from the observed primary γ rays in ^{186}Re. A comparison of the results from the statistical-decay model calculations to the measured γ-ray production cross-section data permitted an evaluation of the adopted decay-scheme data, e.g., spin-parity (J^π) assignments, γ-ray branching ratios, and

*david.a.matters.mil@mail.mil

multipole mixing ratios (δ_γ) for low-lying levels of ^{186}Re. In addition to enriching the data contained in the EGAF, these results represent additions to the Reference Input Parameter Library (RIPL) [15], which is used to generate the Evaluated Nuclear Data File (ENDF) [16] that is employed in a variety of nuclear applications.

II. EXPERIMENT AND DATA ANALYSIS

The experiment was performed at the Prompt Gamma Activation Analysis – Neutron Induced Prompt γ-ray Spectroscopy (PGAA-NIPS) facility at the Budapest Neutron Centre (BNC) in Budapest, Hungary, to examine the prompt γ-ray emissions from ^{186}Re following slow-neutron capture on ^{185}Re. The PGAA-NIPS facility at the BNC is positioned at the terminus of a neutron beamline extending from the 10 MW$_t$ Budapest Research Reactor. The 33.5-m beamline, constructed of 0.75-m long supermirror guide elements, provides an exceptionally low γ-ray background and a well-collimated beam of slow neutrons. The beam guide is slightly curved so that epithermal and fast neutrons, which have wavelengths less than the critical value for reflection, are not transmitted through the guide and do not reach the target. This effectively limits the flux incident on the target to thermal and cold neutrons [17]. In this experiment, neutrons were collimated prior to the target using a set of ^{6}Li-loaded polymer apertures, which defined a beam size of 2 cm $\times$ 2 cm. The total thermal-neutron flux was 1.5×10^7 neutrons cm^{-2} s^{-1}.

The high-purity germanium (HPGe) detector used at the PGAA station is an n-type closed-end coaxial detector with 27% relative efficiency, surrounded by an annular Compton-suppression shield consisting of eight bismuth germanate detector segments. The suppression shield is set in anticoincidence mode with the HPGe detector to eliminate signals due to Compton scattering, so that the Compton background present in the resulting spectra is significantly reduced. The detector is located 23.5 cm from the center of the sample chamber, oriented at 90° to the beam direction. The detector is encased in neutron-absorbing ^{6}Li-loaded polymer sheets in order to keep the beam background low [18]. Further information about the PGAA-NIPS facility can be found in Ref. [19].

The target for the experiment consisted of 150.76 mg of rhenium-metal powder enriched to 96.74% ^{185}Re. The sample was contained in a thin teflon bag, prepared according to the techniques described in Ref. [20]. The sample was then aligned in an aluminum target holder, suspended by thin teflon threads, for placement in the neutron beam at an angle of 30°. Energy and efficiency calibrations of the spectrometer were performed using standard ^{133}Ba, ^{152}Eu, ^{207}Bi, ^{226}Ra, and ^{241}Am calibration sources for low energies. For energies above 1.5 MeV, samples of deuterated urea (CD_4N_2O) and polyvinyl chloride (PVC) were placed in the neutron beam, and prompt γ rays from the ^{14}N$(n,\gamma)^{15}$N and ^{35}Cl$(n,\gamma)^{36}$Cl reactions, respectively, were used to calibrate the spectrometer [21,22].

A. Spectroscopic analysis

Prompt γ-ray spectra from irradiation of the enriched ^{185}Re target were collected at two different gain settings over a 19.14-h period, and the spectra were analyzed offline using the HYPERMET-PC program [23]. A low-gain setting was used to capture the full-scale spectrum ($0 \leqslant E_\gamma \leqslant 6.5$ MeV), such that primary γ rays up to the ^{186}Re neutron-separation energy could be identified. Representative histograms from the low-gain setting are shown in Fig. 1, with a focus on the primary γ-ray peaks in the lower panel of the figure.

The high-gain setting was used to achieve improved resolution in the low-energy ($\leqslant$1.1 MeV) region of the spectrum. This permitted fitting the large number of low-energy peaks and multiplets in the ^{186}Re spectrum. A representative portion of the high-gain spectrum is shown in Fig. 2 with peak fits from HYPERMET-PC. Fitting the particular region shown in the figure was problematic. The 59.0-keV γ ray is the highest-intensity γ ray in the ^{185}Re(n,γ) spectrum, and after correcting for internal conversion it contributes over 80% to the total radiative-capture cross section σ_0, so it was essential that the peak intensity was properly fitted. However, the 59.0-keV γ ray peak is convolved with the 59.7- and 61.1-keV rhenium K_α x rays. The fit of this multiplet was adjusted until the ratio of the intensities for the 59.7- and 61.1-keV K_α x rays was 0.584(13), which matched the ratio 0.584(18) from the x-ray yields in Ref. [24]. The close agreement between these ratios gave a high degree of confidence in the fitted intensity ascribed to the 59.0-keV γ-ray peak.

B. Cross section standardization

Measurement of peak areas in the prompt neutron-capture γ-ray spectra from the enriched ^{185}Re target, corrected for detector efficiency and γ-ray attenuation in the target, provided γ-ray intensities for transitions in ^{186}Re. For these transitions, the partial cross sections σ_γ were determined by standardizing to the known ^{35}Cl(n,γ) comparator cross sections $\sigma_{\gamma,c}$ from Refs. [25,26], listed in Table I. Analysis of a spectrum from the irradiation of a stoichiometric $^{\text{nat}}ReCl_3$ target permitted determination of partial cross sections $\sigma_{\gamma,x}$ for a few strong prompt γ rays from the $^{\text{nat}}$Re(n,γ) reaction using the relation

$$\frac{\sigma_{\gamma,x}}{\sigma_{\gamma,c}} = \frac{n_x}{n_c}\frac{A_{\gamma,x}/\epsilon(E_{\gamma,x})}{A_{\gamma,c}/\epsilon(E_{\gamma,c})}. \quad (1)$$

In Eq. (1), $A_{\gamma,x}$ and $A_{\gamma,c}$ are the peak areas of the unknown and comparator γ rays, respectively, $\epsilon(E_{\gamma,x})$ and $\epsilon(E_{\gamma,c})$ are the detector efficiencies at the γ-ray energies $E_{\gamma,x}$ and $E_{\gamma,c}$, and the known 3 : 1 stoichiometry of the target compound implies $(n_x/n_c) = 1/3$ [27]. The $^{\text{nat}}$Re(n,γ) cross sections obtained using Eq. (1) were then corrected for isotopic abundance ($^{\text{nat}}$Re comprises 37.398% ^{185}Re and 62.602% ^{187}Re [28]) to arrive at isotopic ^{185}Re(n,γ) cross sections. These ^{185}Re(n,γ) cross sections were then used as standards for normalizing the intensities of all prompt γ rays obtained from the enriched ^{185}Re spectrum (Fig. 1).

C. Determination of effective target thickness

Rhenium metal has a density of 21.02 g/cm^3, and therefore has a large photon attenuation cross section for γ rays with energies below 300 keV. As a result, partial cross sections for low-energy γ rays must be corrected for self-absorption within the target mass during standardization. Because the target

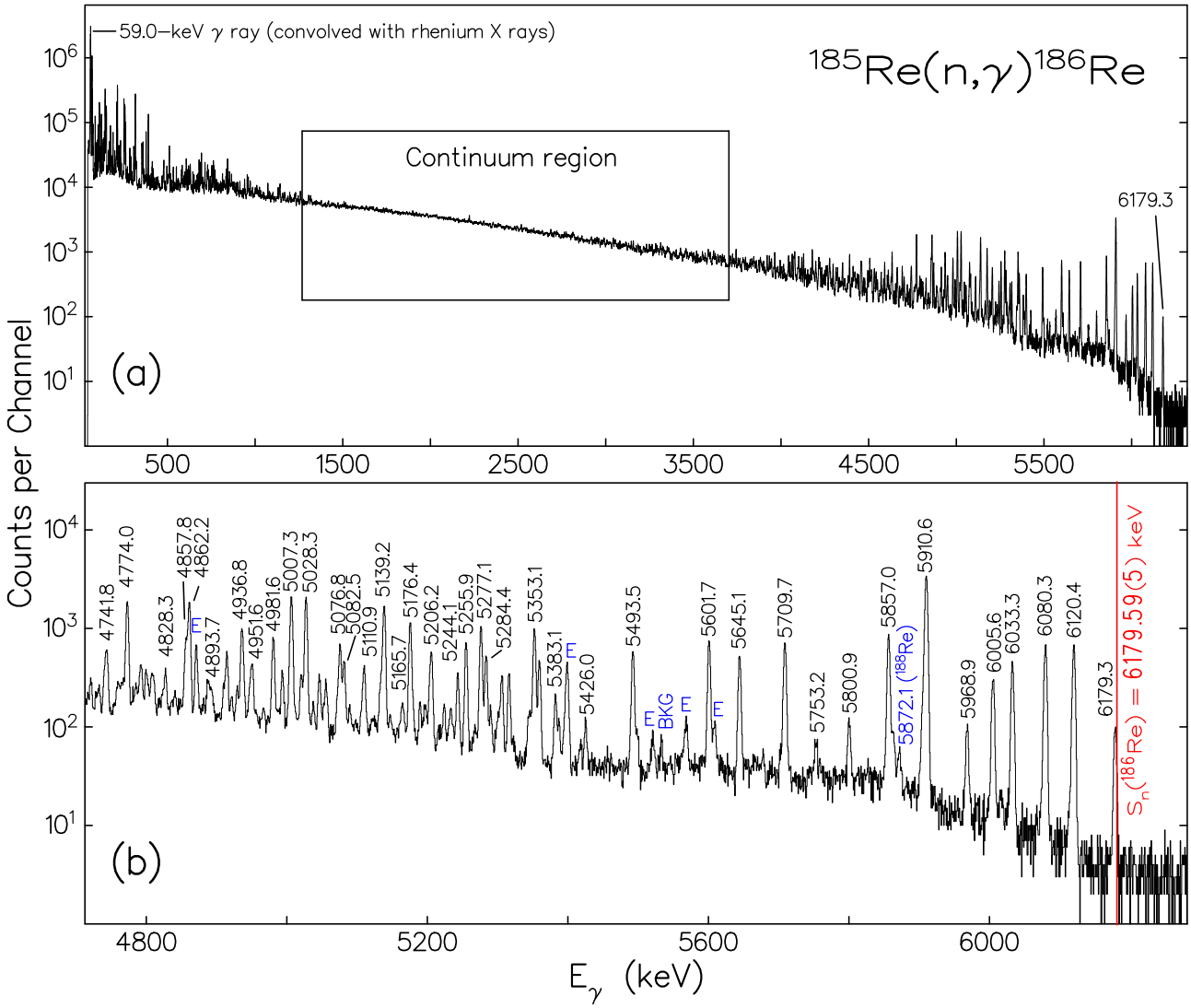

FIG. 1. Representative prompt γ-ray spectra from the ^{185}Re$(n,\gamma)^{186}$Re reaction, with counts shown in logarithmic scale, measured using the low-gain setting. In (a), the entire range of γ-ray energies from ^{186}Re is shown. The peaks from the highest-intensity 59.0-keV γ ray (convolved with rhenium x rays, see Fig. 2 and the text) and the 6179.3-keV primary γ ray from the capture state to the ground state are identified for orientation. The area in the center of the spectrum is the quasicontinuum region, where the level density is so high that transitions to and from levels in this region are unresolvable. In (b), an expansion of the same spectrum in the 4.7–6.5 MeV energy region is shown, in which the majority of γ rays were fitted. The highest-intensity primary γ rays from ^{186}Re are labeled in black, while escape peaks (E), background (BKG), and contaminant γ rays from neutron capture on ^{188}Re are identified in blue. The ^{186}Re neutron separation energy $S_n = 6179.59(5)$ keV determined in this work is identified with a red vertical line.

sample is of nonuniform thickness, it is difficult to accurately describe its geometry using particle-transport simulations. An alternative method involves comparing partial cross sections for low-energy γ rays, corrected for attenuation using an effective target thickness, with reference values obtained from irradiation of an optically-thin target sample. By adjusting the effective thickness to minimize the residual errors between the thick-target cross sections and the reference cross sections from the thin target, an effective thickness for the enriched ^{185}Re target can be found that can be used to calculate the attenuation at any γ-ray energy [29].

To determine the effective thickness of the enriched ^{185}Re target, a prompt γ-ray spectrum from irradiation of a lower-density hydrated rhenium chloride sample [27] was measured. The density of this sample was such that γ-ray self-absorption within the material was minimal and could be neglected. The comparator cross sections from ^{35}Cl(n,γ) in Table I were used to standardize the ^{185}Re(n,γ) cross sections using Eq. (1). Standard partial cross sections (σ_γ^S) for the four strong, well-resolved γ-ray transitions in ^{186}Re listed in Table I were extracted and compared with the cross sections for the same γ rays obtained from the thick enriched ^{185}Re target (σ_γ^T).

For a given γ ray produced in the target with intensity I_0, measured at the detector with intensity I_γ, the γ-ray attenuation factor is given by I_γ/I_0. The attenuation factor depends on the γ-ray energy E_γ and the target thickness

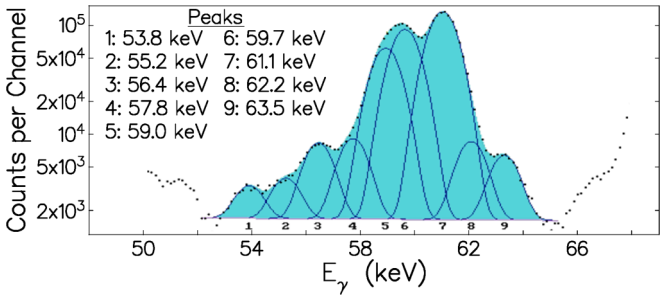

FIG. 2. Representative section of the prompt γ-ray spectrum using the high-gain setting to show the quality of the fits performed using HYPERMET-PC. Black dots identify the experimental counts in logarithmic scale, while the shaded region is the result of the least-squares fit, and solid blue lines identify the fits of each peak in the 52- to 65-keV energy range.

t, and is obtained by integrating the exponential-attenuation law $I_\gamma/I_0 = \exp(-\mu_\gamma x)$ over the depth x to arrive at the expression

$$\frac{I_\gamma(E_\gamma,t)}{I_0} = \frac{\cos\theta}{t\rho\left(\frac{\mu_\gamma}{\rho}\right)_{E_\gamma}}\left[1-\exp\left(\frac{-t\rho\left(\frac{\mu_\gamma}{\rho}\right)_{E_\gamma}}{\cos\theta}\right)\right]. \quad (2)$$

In Eq. (2), $(\mu_\gamma/\rho)_{E_\gamma}$ is the γ-ray mass-attenuation coefficient at the γ-ray energy E_γ, ρ is the target sample density, and θ is the angle at which the sample face is oriented relative to the detector face [2,29]. In the experiment described in this work, $\theta = 30^\circ$, and mass-attenuation coefficients used in the calculations were taken from the XMUDAT database [30]. After correcting for attenuation and detector efficiency, the peak areas $A_{\gamma,x}$ from the thick target should be directly proportional to the thin-target standard cross sections σ_γ^S, i.e., the following relation should hold for all E_γ for a constant C:

$$\frac{\sigma_\gamma^S}{A_{\gamma,x}/\epsilon(E_{\gamma,x})}\cdot\frac{I_\gamma(E_\gamma,t)}{I_0} = C. \quad (3)$$

The effective sample thickness t for the enriched ^{185}Re target in Eq. (3) was varied until C converged to a unique value for the 103.3-, 214.7-, 255.0-, and 391.0-keV γ rays. The errors about the mean value of C for each thickness were analyzed using the χ^2-minimization procedure outlined by Hurst *et al.* in Ref. [29]. Two parameters, the thickness t and a global correlation coefficient (see Ref. [29] for details), were adjusted to minimize the χ^2 to fit the four data points, leaving two degrees of freedom (ndf = 2). A plot of the χ^2 values as a function of thickness t is shown in Fig. 3, where it is evident that the minimum ($\chi^2_{\min}$) is achieved at an effective thickness of $t = 0.086$ mm. The 1σ-uncertainty range for a 2-parameter adjustment is defined by $\chi^2_{\min} + 2.3$ [31], which results in an uncertainty of ± 0.008 mm in the effective thickness.

TABLE I. Elemental comparator cross sections $\sigma_{\gamma,c}$ for ^{35}Cl(n,γ) from Refs. [25,26] used in the analysis of the prompt γ-ray spectrum from $^{\text{nat}}$ReCl$_3(n,\gamma)$ to determine standard isotopic ^{185}Re(n,γ) cross sections σ_γ^S, also listed.

Source (isotope; reaction)	E_γ (keV)	$\sigma_{\gamma,c}$, σ_γ^S (b)
^{36}Cl; ^{35}Cl(n,γ)	517.1	7.58(5)
^{36}Cl; ^{35}Cl(n,γ)	788.4	5.42(5)
^{36}Cl; ^{35}Cl(n,γ)	1164.9	8.91(4)
^{36}Cl; ^{35}Cl(n,γ)	1951.1	6.33(4)
^{36}Cl; ^{35}Cl(n,γ)	5715.2	1.820(16)
^{186}Re; $^{\text{nat}}$ReCl$_3(n,\gamma)$	103.3	1.34(8)
^{186}Re; $^{\text{nat}}$ReCl$_3(n,\gamma)$	214.7	6.6(4)
^{186}Re; $^{\text{nat}}$ReCl$_3(n,\gamma)$	255.0	3.19(19)
^{186}Re; $^{\text{nat}}$ReCl$_3(n,\gamma)$	391.0	3.27(6)

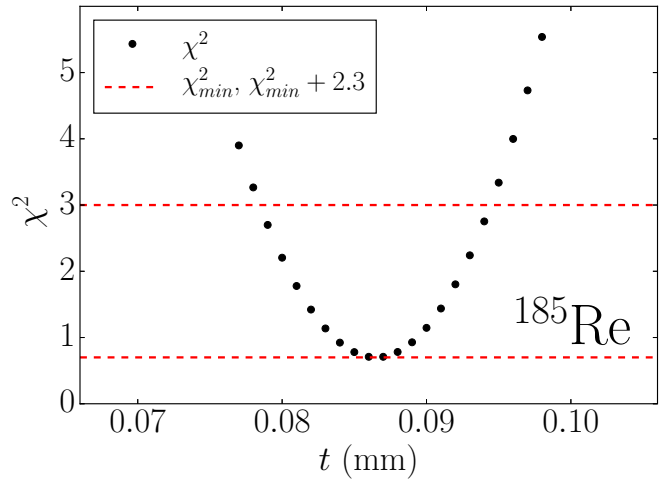

FIG. 3. Plot of the global χ^2 values as a function of target thickness for the enriched ^{185}Re sample. The lower dashed-red line corresponds to the minimum of the global χ^2 distribution, which occurs at an effective thickness of 0.086 mm. The upper dashed-red line is drawn at $\chi^2_{\min} + 2.3$, which defines the 1σ range of [0.078 mm,0.094 mm] of acceptable t values for two adjustable parameters [31].

The ratio of the partial cross sections from the attenuated thick-target sample, σ_γ^T, to the unattenuated thin-target values σ_γ^S, yields an experimental attenuation factor:

$$\left(\frac{I_\gamma}{I_0}\right)_{\text{exp}} = \frac{\sigma_\gamma^T}{\sigma_\gamma^S}. \quad (4)$$

To illustrate the effectiveness of the χ^2-minimization procedure at producing an accurate effective thickness, the experimental attenuation factors $(I_\gamma/I_0)_{\text{exp}}$ for comparator and other low-energy ^{186}Re γ rays were compared against the attenuation factors calculated using Eq. (2) with an assumed thickness of $t = 0.086$ mm, with the same calculations performed at thicknesses of 0.078 mm and 0.094 mm to obtain the $\pm 1\sigma$ uncertainty band. The good agreement in the resulting plot, shown in Fig. 4, validates the effective thickness found for the enriched ^{185}Re target. The calculated attenuation factors were used to correct the ^{185}Re(n,γ) cross sections obtained using Eq. (1) at all γ-ray energies. Uncertainties in the attenuation factors were propagated through the calculations of the γ-ray production cross sections presented in this work.

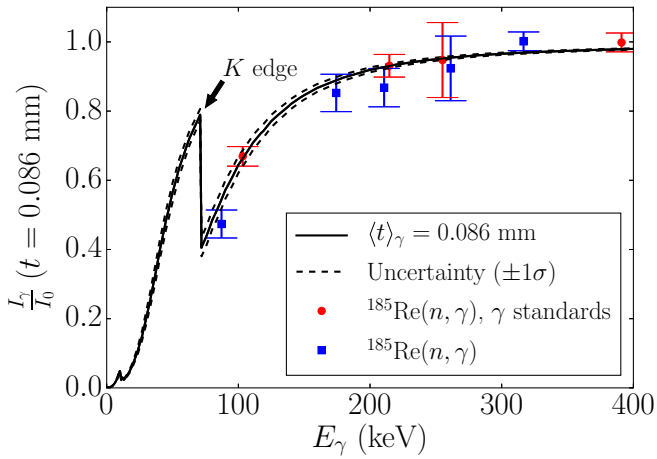

FIG. 4. Plot of the attenuation factor I_γ/I_0 at an effective thickness of 0.086 mm (solid black line with dashed lines indicating uncertainty) with the experimental ratios of thick-target partial cross sections to thin-target partial cross sections, $\sigma_\gamma^T/\sigma_\gamma^S = (I_\gamma/I_0)_{\rm exp}$. The data points identified by red circles are for the well-resolved 103.3-, 214.7-, 255.0-, and 391.0-keV γ rays, which were used as standards to determine the effective thickness. Shown for comparison are the 87.2-, 174.3-, 210.7-, 261.2-, and 316.6-keV γ-ray transitions in ^{186}Re (blue-square data points), which are not as well-resolved in the spectra and could not be used for determining the effective thickness.

III. STATISTICAL MODELING

A significant portion of the results presented in this work is based on a combination of experimental results with simulations of γ decay following thermal-neutron capture, based on a statistical model of the nucleus. The Monte Carlo statistical-decay code DICEBOX [32], which assumes a generalization of the extreme statistical model of compound nucleus formation and decay [33], was used for these simulations.

To model the thermal-neutron capture cascade, DICEBOX simulates numerous (n,γ) decay-scheme simulations, known as nuclear realizations. Each realization is based on a statistical model of the level density $\rho(E,J,\pi)$ and γ-ray transition widths Γ_{if} for the formation and decay of the compound nucleus. To describe the decay scheme, all level energies, spin-parity assignments, and depopulating γ rays below a user-defined cutoff excitation energy (referred to as the critical energy E_c) are taken from the experimental-decay scheme. For levels in the quasicontinuum, defined in this case as the levels above E_c, the code generates a random set of levels according to an *a priori* assumed model of the level density (LD). Transitions to and from these levels to low-lying levels below E_c are randomly generated according to an *a priori* assumed model of the photon strength function (PSF), where angular-momentum selection rules are applied to determine allowed transitions. The PSFs, $f^{(XL)}(E_\gamma)$, for transitions with multipolarity $X = E$ (electric) or M (magnetic) and multipole order L, are used to describe statistical γ decay. For allowed transitions, the partial radiation widths Γ_{if}^{XL} of the transition probabilities from initial state i to final state f are assumed to follow a Porter-Thomas distribution [34]

$$P(x) = \frac{1}{\sqrt{2\pi x}} e^{-x/2}, \tag{5}$$

where $x = \Gamma_{if}^{XL}/\langle\Gamma_{if}^{XL}\rangle$, and the mean value $\langle\Gamma_{if}^{XL}\rangle$ is given by

$$\left\langle\Gamma_{if}^{XL}\right\rangle = \frac{f^{(XL)}(E_\gamma)\cdot E_\gamma^{2L+1}}{\rho(E_i,J_i,\pi_i)}. \tag{6}$$

Here $\rho(E_i,J_i,\pi_i)$ is the level density at an initial state E_i characterized with a spin-parity $J_i^{\pi_i}$ [35]. γ-ray transition probabilities are corrected for internal conversion using coefficients calculated with the Band-Raman Internal Conversion Calculator (BRICC) version 2.3S code [36,37]. Primary γ rays (i.e., those that originate at the capture state) feeding discrete levels below E_c are also taken from experiment. In order to obtain accurate probabilities of populating discrete levels below E_c with uncertainties (due to statistical Porter-Thomas fluctuations) small enough for comparison with experimental cross sections, 50 nuclear realizations were simulated for each PSF/LD model combination, with 100,000 γ-ray cascades simulated per realization [7].

1. Level densities

The nuclear-level density models used in this work were assumed to be functions of excitation energy E, spin J, and parity π, with the general form

$$\rho(E,J,\pi) = \rho(E)f(J)\pi(E), \tag{7}$$

where $\rho(E)$ is the total level density at excitation energy E, $f(J)$ is a spin-distribution factor, and $\pi(E)$ is the parity distribution identifying the fraction of positive- or negative-parity states as a function of excitation energy. Two different $\rho(E,J) = \rho(E)f(J)$ models were considered in the statistical-model calculations, the constant-temperature formula (CTF) [38] and the backshifted Fermi gas (BSFG) [38,39] models.

The CTF LD model assumes a constant nuclear temperature T, and is given by

$$\rho(E,J) = \frac{f(J)}{T}\exp\left(\frac{E-E_0}{T}\right), \tag{8}$$

where E_0 is an energy backshift related to the nucleon pairing energy. The spin-distribution factor $f(J)$ is

$$f(J) = \frac{2J+1}{2\sigma_c^2}\exp\left[-\frac{(J+1/2)^2}{2\sigma_c^2}\right], \tag{9}$$

where σ_c is a spin cutoff factor. For a nucleus with mass number A, the formula $\sigma_c = 0.98A^{0.29}$ was adopted for the spin cutoff factor in the CTF LD model [40].

The BSFG LD model assumes the nucleus to be a two-component fermionic fluid, which leads to the expression

$$\rho(E,J) = f(J)\frac{\exp[2\sqrt{a(E-E_1)}]}{12\sqrt{2}\sigma_c a^{1/4}(E-E_1)^{5/4}}, \tag{10}$$

TABLE II. Level density parameters for the CTF (T and E_0) and BSFG (a and E_1) models used in statistical-model calculations to model γ-ray cascades in ^{186}Re. The parameters were taken to be the mean values quoted from the respective references.

Reference	T (MeV)	E_0 (MeV)	a (MeV^{-1})	E_1 (MeV)
[40]	0.56(1)	−1.76(18)	19.87(28)	−0.90(10)
[41]	0.54(1)	−1.59(15)	18.19(25)	−0.82(8)

where E_1 is an energy backshift. The spin-cutoff factor σ_c for the BSFG model was taken as

$$\sigma_c^2 = 0.0146A^{5/3}\frac{1+\sqrt{1+4a(E-E_1)}}{2a}, \tag{11}$$

and a is a shell-model level-density parameter [40].

The parameters T, E_0, a, and E_1 in Eqs. (8), (10), and (11) were assumed to follow the parametrizations of von Egidy and Bucurescu in Refs. [40] or [41], and are listed in Table II.

We tested both a parity-independent [$\pi(E) = 1/2$] LD model as well as a LD model slightly dependent on parity at low excitation energies, described by Al-Quraishi *et al.* in Ref. [42]. In the parity-dependent LD model, the function $\pi(E)$ is a Fermi-Dirac distribution describing the fraction of positive- or negative-parity states (depending on the sign used in the distribution function) as a function of E. The functional form for $\pi(E)$ is

$$\pi(E) = \frac{1}{2}\left(1 \pm \frac{1}{1+\exp[c(E-\delta_p)]}\right), \tag{12}$$

where the sign of the $\pm$ is determined from the parity of the ground state, c is a spin-cutoff factor, and δ_p is an energy shift. For ^{186}Re, when $\pi(E)$ represents the distribution of positive-parity states, a negative sign is used in Eq. (12) to signify that low-energy levels have predominantly negative parity. For the statistical-model calculations, we assumed the parametrization $\delta_p = -0.1814$ MeV and $c = 3.0$ MeV^{-1} from Ref. [42].

2. *Photon strength functions*

For the transitions relevant to the statistical modeling of thermal-neutron capture γ-ray cascades, the $E1$ PSF (which dominates γ decay for $E_\gamma \geqslant 4$ MeV) is believed to be described by the low-energy tail of the giant dipole electric resonance (GDER). Above $E_\gamma \approx 8$ MeV, the shape of the $E1$ PSF can be probed using (γ,n) measurements. At these higher energies, the shape of the $E1$ PSF for deformed nuclei is usually well described by a sum of two standard Lorentzians, sometimes known as the Brink-Axel (BA) model [43,44]. At γ-ray energies below ~8 MeV, the shape of the $E1$ PSF is not well known, and several extrapolations of the BA model are typically used. In addition to the BA model, we tested the Kadmenski, Markushev, and Furman (KMF) [45], generalized Lorentzian (GLO) [46], and modified generalized Lorentzian (MGLO) [47] models for the $E1$ PSF in this work.

The Brink-Axel function $f_{\rm BA}^{(E1)}(E_\gamma)$ for the $E1$ PSF in deformed nuclei is a sum of two standard Lorentzians, corresponding to vibration modes along and perpendicular to the nuclear-symmetry axis:

$$f_{\rm BA}^{(E1)}(E_\gamma) = \frac{1}{3(\pi\hbar c)^2}\sum_{i=1}^{2}\frac{\sigma_{G_i}E_\gamma\Gamma_{G_i}^2}{\left(E_\gamma^2-E_{G_i}^2\right)^2+E_\gamma^2\Gamma_{G_i}^2}. \tag{13}$$

TABLE III. Resonance parameters for the GDER and GQER used in statistical-model calculations to model γ-ray cascades in ^{186}Re. The GDER parameters are from Ref. [49], and the GQER parameters are from a theoretical global parametrization for isovector-isoscalar vibrations described in the text.

Resonance	E_{G_1} (MeV)	Γ_{G_1} (MeV)	σ_{G_1} (mb)	E_{G_2} (MeV)	Γ_{G_2} (MeV)	σ_{G_2} (mb)
GDER	12.63	2.77	279	15.24	4.69	375
GQER	11.04	3.88	4.64	–	–	–

The parameters E_{G_i} and Γ_{G_i} represent the resonant energies and widths of the GDER vibration modes, and the σ_{G_i} are the resonance cross sections. These values are tabulated in the RIPL [15] for a variety of stable isotopes, and the systematics are such that the parameter values are relatively constant for nuclei with similar deformation in a given mass region. In our case we adopted values obtained from a least-squares fit of $^{\rm nat}$Re photoabsorption data [48] over the interval 10.8 − 18.8 MeV [49]. The resulting GDER parameters, listed in Table III, are adopted in the RIPL [15] and were used in the statistical-model calculations described in this work.

The BA model is dependent on E_γ alone, while other $E1$ PSF models considered in this work (KMF, GLO, MGLO) also include an additional temperature dependence, due to the inclusion of a temperature-dependent resonance width given by

$$\Gamma_{G_i}(E_\gamma,\Theta) = \frac{\Gamma_{G_i}}{E_{G_i}^2}\left(E_\gamma^2+4\pi^2\Theta^2\right). \tag{14}$$

In Eq. (14) the nuclear temperature Θ is a function of the excitation energy E_f of the final state, level density parameter a from Ref. [40], and a pairing energy Δ:

$$\Theta = \sqrt{(E_f-\Delta)/a}. \tag{15}$$

The pairing energy is determined for odd-odd nuclei via the formula $\Delta = -0.5|P_d|$, where P_d is the deuteron-pairing energy found in Ref. [40]. For ^{186}Re, $P_d = -1.492$ MeV and $\Delta = -0.796$ MeV.

For deformed nuclei, the KMF model of the $E1$ PSF is given by the equation

$$f_{\rm KMF}^{(E1)}(E_\gamma,\Theta) = \frac{1}{3(\pi\hbar c)^2}\sum_{i=1}^{2}F_K\frac{\sigma_{G_i}\Gamma_{G_i}E_\gamma\Gamma_{G_i}(E_\gamma,\Theta)}{\left(E_\gamma^2-E_{G_i}^2\right)^2}, \tag{16}$$

where the dimensionless Fermi liquid parameter F_K is taken to have a value of 0.7 [50] in this work.

An empirical model, connecting the KMF at low E_γ with the BA model near the GDER maximum was proposed by Kopecky and Uhl in Ref. [46]. This model, called the GLO,

has the functional form

$$f^{(E1)}_{\rm GLO}(E_\gamma,\Theta) = \sum_{i=1}^{2} \frac{\sigma_{G_i}\Gamma_{G_i}}{3(\pi\hbar c)^2}\left[F_K\frac{4\pi^2\Theta^2\Gamma_{G_i}}{E^5_{G_i}} + \frac{E_\gamma\Gamma_{G_i}(E_\gamma,\Theta)}{\left(E^2_\gamma - E^2_{G_i}\right)^2 + E^2_\gamma\Gamma^2_{G_i}(E_\gamma,\Theta)}\right] \quad (17)$$

with terms as defined in the BA and KMF models above.

A generalization of the GLO model to describe deformed nuclei was later proposed by Kopecky *et al.* in Ref. [51]. This model, referred to as the enhanced generalized Lorentzian (EGLO), includes an enhanced resonance width

$$\Gamma'_{G_i}(E_\gamma,\Theta) = \left[k_0 + (1-k_0)\frac{E_\gamma - E_0}{E_{G_i} - E_0}\right]\Gamma_{G_i}(E_\gamma,\Theta), \quad (18)$$

where the energy shift $E_0 = 4.5$ MeV [51], and the parameter k_0 can be adjusted to achieve optimum agreement with the experimental photoabsorption cross-section data. The MGLO model [47] considered in this work modifies the behavior of the EGLO [51] at low γ-ray energies, and is obtained from Eq. (17) by replacing the temperature-dependent resonance width $\Gamma_{G_i}(E_\gamma,\Theta)$ in Eq. (14) with the enhanced resonance width from Eq. (18).

The four $E1$ PSF models considered in this work are shown in Fig. 5 with the (γ,n) data from Ref. [48]. As evident, the KMF and GLO models (which were originally proposed for spherical nuclei) do not reproduce the (γ,n) data in the range $8 \leqslant E_\gamma \leqslant 10$ MeV. On the other hand, an enhancement of $k_0 = 2.9$ in the MGLO model results in a good fit to the experimental photoabsorption data in the low-energy tail of the GDER. For this reason, we assumed an enhancement factor of 2.9 for all calculations in which the MGLO model was used for the $E1$ PSF.

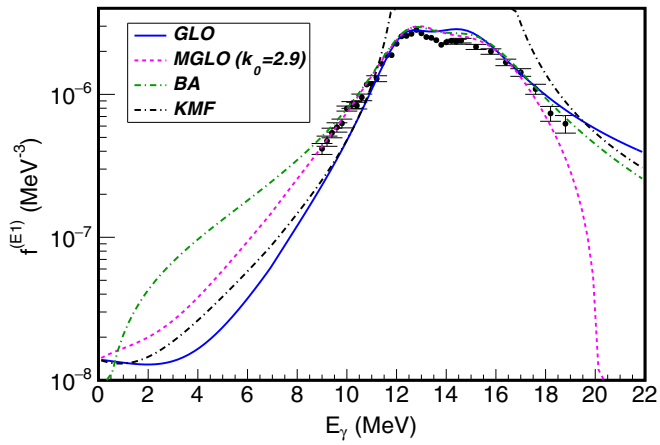

FIG. 5. Experimental (γ,n) data from Ref. [48] overlaid with the BA, GLO, MGLO, and KMF models for the $E1$ PSF for transitions from the capture state. The resonance parameters used in each model are from Ref. [49]. The value of 2.9 for the enhancement factor k_0 in the MGLO model was chosen based on the observed agreement between the MGLO and the experimental cross-section data in the low-energy tail of the GDER.

The single-particle (SP) model for the $M1$ PSF was adopted in this work. Statistical-decay modeling of the tungsten isotopes ^{183,185,187}W, similar in mass to ^{186}Re, found that a value of $f^{(M1)}_{SP} = 1\times10^{-9}$ MeV^{-3} produced the best agreement between the predictions of the statistical model and the experimental cross sections and total radiative capture width [3]. The same effect was observed for ^{186}Re, so a SP strength of 1×10^{-9} MeV^{-3} was adopted for the calculations in this work. The scissors model [52] for the $M1$ PSF was also considered in this work. Due to the relative insignificance of $M1$ transitions in the statistical-model calculations, the scissors model produced results that were consistent with those of the SP model.

The contribution of $E2$ transitions is much smaller than that of dipole transitions. The GQER model, which uses a standard Lorentzian (SLO) with a single resonance to describe an isovector-isoscalar quadrupole vibration, was used for the $E2$ PSF:

$$f^{(E2)}_{\rm SLO}(E_\gamma) = \frac{1}{5(\pi\hbar c)^2}\frac{\sigma_{G_1}E_\gamma\Gamma^2_{G_1}}{\left(E^2_\gamma - E^2_{G_1}\right)^2 + E^2_\gamma\Gamma^2_{G_1}}. \quad (19)$$

The resonance parameters E_{G_1}, Γ_{G_1}, and σ_{G_1} for the GQER that were used in the statistical-model calculations in this work are listed in Table III. These values were calculated using the following global parametrization: $E_{G_1} = 63A^{-1/3}$ [53], $\Gamma_{G_1} = 6.11 - 0.012A$ [54], and $\sigma_{G_1} = 1.5\times10^{-4}\frac{Z^2E^2_{G_1}A^{-1/3}}{\Gamma_{G_1}}$ [54].

The strengths of $M2$ and higher-multipole transitions are expected to be negligible in the statistical-decay modeling, and were not considered in modeling the neutron-capture γ cascade in this work.

3. *Calculation of the total radiative thermal-neutron capture cross section*

DICEBOX models the contribution to the total (n,γ) cross section from the quasicontinuum, and calculates the probability per neutron capture of direct feeding of the ground state from the quasicontinuum (P_0). The total radiative-capture cross section σ_0 is obtained by combining this contribution with the experimentally-measured partial γ-ray production cross sections from discrete levels below E_c feeding the ground state directly ($\sigma_{\gamma 0}$), using the expression

$$\sigma_0 = \sum\sigma^{\rm exp}_{\gamma 0} + \sum\sigma^{\rm sim}_{\gamma 0} = \frac{\sum\sigma^{\rm exp}_{\gamma 0}}{1-P_0}. \quad (20)$$

In Eq. (20), the superscripts 'exp' and 'sim' refer to the experimental and simulated cross sections, corrected for internal conversion, directly feeding the ground state from the discrete levels below E_c and from the quasicontinuum, respectively [3].

IV. RESULTS AND DISCUSSION

Partial γ-ray production cross sections for 106 γ rays deexciting and feeding 48 discrete levels from the adopted level scheme (Ref. [10]) up to an excitation energy of 864.7 keV are listed in Table IV, along with 102 primary γ rays feeding

TABLE IV. Experimental thermal-neutron capture partial γ-ray production cross sections σ_γ from the ^{185}Re(n,γ) reaction. Spin-parity assignments $J_{i,f}^{\pi_{i,f}}$ were taken from the ENSDF adopted levels for ^{186}Re [10], except those values in bold, which are proposed in this work on the basis of statistical-decay modeling results. Transition multipolarities XL are from the ENSDF [10], with those identified with square brackets assumed from angular-momentum selection rules and the values proposed in this work in bold text. Tentative values are identified with parentheses. Level excitation energies $E_{i,f}$ were obtained from a least-squares fit to the γ-ray energies E_γ measured in this work, unless otherwise noted. Internal conversion coefficients α were calculated using BRICC [36] using the mean or limiting values of the mixing ratios δ_γ taken from the ENSDF [10], unless otherwise noted.

E_i (keV)	$J_i^{\pi_i}$	E_f (keV)	$J_f^{\pi_f}$	E_γ (keV)	σ_γ (b)	α	XL	δ_γ
0.0	1^-							
59.007(6)	2^-	0.0	1^-	58.987(6)	17.5(11)	4.14	$M1$	
99.381(7)	3^-	59.007(6)	2^-	40.364(7)[a]	2.2(5)	15.59	$M1+E2$	0.11(2)
		0.0	1^-	99.449(11)	0.47(9)	4.21	$E2$	
146.227(9)	3^-	59.007(6)	2^-	87.199(8)[b]	2.38(14)	7.66	$M1$	
		0.0	1^-	146.57(16)[a]	0.20(4)	0.95	$[E2]$	
174.059(11)	4^-	99.381(7)	3^-	74.685(11)[c]	0.95(7)	11.96	$M1+E2$	0.19(6)
$\sim$186	6^-	174.059(11)	4^-	($\sim$12)[d,i]	$\leqslant 7\times10^{-5}$	7.1×10^4	$[E2]$	
		148.2(5)[f]	8^+	($\sim$38)[d,i]	$\leqslant 5\times10^{-3}$	1.0×10^3	$[M2]$	
210.722(10)	2^-	146.227(9)	3^-	64.42(4)[d,e]	0.051(9)	3.20	$[M1]$	
		99.381(7)	3^-	111.16(8)[a]	1.28(18)	3.82	$M1$	
		59.007(6)	2^-	151.722(14)	2.45(14)	0.84	$E2(+M1)$	
		0.0	1^-	210.705(23)	3.05(18)	0.58	$M1(+E2)$	$\leqslant$0.39
268.729(12)	4^-	146.227(9)	3^-	122.519(12)	1.82(13)	2.89	$[M1]$	
		99.381(7)	3^-	169.46(3)[a]	0.36(9)	0.78	$E2(+M1)$	$\geqslant$1.3
		59.007(6)	2^-	209.78(4)	0.41(4)	0.27	$[E2]$	
273.566(12)	4^-	174.059(11)	4^-	99.449(11)[a]	0.30(7)	5.25	$[M1]$	
		146.227(9)	3^-	127.354(16)[a]	0.76(17)	1.84	$M1+E2$	$1.8(^{+86}_{-7})$
		99.381(7)	3^-	174.31(3)	1.11(7)	0.74	$M1+E2$	$1.2(^{+7}_{-4})$
313.989(12)	3^+	210.722(10)	2^-	103.290(12)	1.34(8)	0.35	$[E1]$	
		146.227(9)	3^-	167.657(17)	0.57(3)	0.10	$(E1)$	
		99.381(7)	3^-	214.677(23)	6.6(4)	0.05	$E1$	
		59.007(6)	2^-	255.04(3)	3.19(19)	0.04	$E1$	
316.531(19)	1^-	59.007(6)	2^-	257.50(3)	3.11(18)	0.30	$M1+E2$	0.60(22)
		0.0	1^-	316.58(4)	5.63(16)	0.21	$M1$	
317.792(19)	5^-	174.059(11)	4^-	143.88(3)	1.6(2)	1.25	$M1+E2$	$1.6(^{+12}_{-5})$
322.488(15)	3^-	210.722(10)	2^-	111.65(3)[a]	1.4(3)	3.77	$[M1]$	
		174.059(11)	4^-	148.92(7)[a]	0.082(20)	1.66	$[M1]$	
		146.227(9)	3^-	176.32(3)[a]	0.38(8)	1.03	$(M1,E2)$	
		99.381(7)	3^-	223.05(3)	0.50(3)	0.38	$M1+E2$	$1.02(^{+29}_{-22})$
		59.007(6)	2^-	263.14(7)[a]	0.23(5)	0.34	$[M1]$	
$\sim$330	5^+	$\sim$186	6^-	144.230(22)	2.6(3)	0.15	$E1$	
351.25(3)	**4^+**	146.227(9)	3^-	205.14(9)[a]	0.056(15)	0.06	$[E1]$	
		99.381(7)	3^-	251.87(3)	4.3(3)	0.04	$E1$	
378.535(18)	2^-	316.531(19)	1^-	62.22(4)[a]	1.11(17)	3.55	$M1(+E2)$	$\leqslant$1.0[l]
		146.227(9)	3^-	232.16(3)[h]	0.55(6)	0.48	$[M1]$	
		59.007(6)	2^-	319.48(4)	0.368(23)	0.20	$[M1]$	
		0.0	1^-	378.49(5)	1.52(9)	0.13	$M1$	
417.784(21)	**5^-**	273.566(12)	4^-	144.230(22)[c]	0.075(4)	1.82	$[M1]$	
		268.729(12)	4^-	148.92(7)	0.57(10)	1.21	$M1+E2$	$1.2(^{+8}_{-4})$
		146.227(9)	3^-	271.56(4)[a]	0.23(7)	0.12	$[E2]$	
420.51(3)	4^+	313.989(12)	3^+	106.58(3)[c]	0.91(11)	3.48	$M1+E2$	$1.7(^{+37}_{-7})$
425.70(3)	**4^+**	313.989(12)	3^+	111.65(3)	1.1(4)	3.77	**$[M1]$**	
462.914(18)	5^-	317.792(19)	5^-	145.131(8)[d,e]	0.068(21)	1.79	$[M1]$	
		273.566(12)	4^-	189.270(20)[a]	0.48(12)	0.62	$M1+E2$	$1.0(^{+4}_{-3})$
		268.729(12)	4^-	193.83(16)[h]	0.142(8)	0.79	$[M1]$	
		174.059(11)	4^-	289.32(8)[a]	0.044(13)	0.26	$[M1]$	
		99.381(7)	3^-	363.56(5)	0.239(17)	0.05	$[E2]$	

TABLE IV. (*Continued.*)

E_i (keV)	$J_i^{\pi_i}$	E_f (keV)	$J_f^{\pi_f}$	E_γ (keV)	σ_γ (b)	α	XL	δ_γ
469.945(19)	4^-	322.488(15)	3^-	147.460(19)[h]	1.03(3)	1.71	$(M1+E2)$	
		268.729(12)	4^-	201.16(3)[a]	0.19(4)	0.59	$[M1]$	
		174.059(11)	4^-	296.03(5)	0.141(11)	0.25	$M1$	
470.755(21)	3^-	378.535(18)	2^-	92.104(21)[a]	0.59(13)	6.03	$M1(+E2)$	$\leqslant 1.4$
		322.488(15)	3^-	148.09(6)[d,e]	0.040(12)	1.69	$[M1]$	
		268.729(12)	4^-	202.64(4)[a]	0.040(12)	0.70	**[*M1*]**	
		59.007(6)	2^-	411.52(7)	0.321(24)	0.10	$[M1]$	
~471	**6^+**	~330	5^+	141.31(4)	0.285(23)	1.55	$M1+E2$	$0.9(^{+9}_{-5})$
497.20(4)	6^-	317.792(19)	5^-	179.41(3)	0.23(4)	0.98	$[M1]$	
500.74(6)	**5^+**	351.25(3)	**4^+**	149.57(8)[a]	0.8(4)	1.06	$M1+E2$	$1.8(^{+13}_{-5})$
		99.381(7)	3^-	401.29(7)	0.101(10)	0.37	**[*M2*]**	
534.32(5)	4^-	273.566(12)	4^-	259.84(9)[g]	0.76(16)	0.35	$[M1]$	
		174.059(11)	4^-	360.53(5)	0.95(6)	0.15	$M1$	
549.16(5)	**5^+**	425.70(3)	**4^+**	123.46(3)[c]	0.38(5)	2.27	$M1(+E2)$	$\leqslant 1.1$
559.96(4)	5^+	425.70(3)	**4^+**	134.16(4)	0.067(8)	2.23	**[*M1*]**	
		420.51(3)	4^+	139.61(5)	0.37(6)	1.34	$M1+E2$	$1.8(^{+46}_{-7})$
~562	6^+	~330	5^+	232.16(3)[h]	0.18(4)	0.48	$[M1]$	
577.87(3)	2^-	378.535(18)	2^-	199.81(13)[c]	0.62(21)	0.72	$[M1]$	
		316.531(19)	1^-	261.23(3)	1.16(19)	0.35	$(M1)$	
588.92(3)	4^-	470.755(21)	3^-	118.173(13)	0.49(3)	3.21	$[M1]$	
601.82(4)	1^+	316.531(19)	1^-	285.29(4)	0.59(4)	0.03	$(E1)$	
		210.722(10)	2^-	391.01(5)	3.27(6)	0.01	$E1$	
623.97(5)	1^-	322.488(15)	3^-	300.51(13)[a]	0.14(5)	0.09	**[*E2*]**	
		210.722(10)	2^-	413.39(5)	0.42(3)	0.10	**[*M1*]**	
646.26(4)	5^-	469.945(19)	4^-	176.32(3)	0.37(9)	1.03	$(M1,E2)$	
		317.792(19)	5^-	328.42(20)[d,e]	0.078(23)	0.19	$[M1]$	
658.27(4)	2^+	601.82(4)	1^+	56.445(18)[a]	0.10(3)	29.59	$M1(+E2)$	$\leqslant 1.1$
		322.488(15)	3^-	335.67(15)[a]	0.046(16)	0.02	$[E1]$	
		316.531(19)	1^-	340.969(11)	0.111(12)	0.02	$[E1]$	
665.23(6)	**6^+**	500.74(6)	**5^+**	164.490(24)[c]	0.13(3)	0.89	$M1+E2$	$1.19(^{+29}_{-22})$
680.21(4)	**2^-**	322.488(15)	3^-	357.77(5)	0.305(20)	0.15	**[*M1*]**	
		210.722(10)	2^-	469.38(7)[h]	0.174(16)	0.07	**[*M1*]**	
		0.0	1^-	680.34(15)	0.58(13)	0.03	**[*M1*]**	
686.20(3)	3^-	577.87(3)	2^-	108.315(18)[a]	0.18(4)	4.11	$[M1]$	
		470.755(21)	3^-	215.28(15)[d,e]	0.098(24)	0.59	$[M1]$	
		378.535(18)	2^-	307.69(4)	0.70(5)	0.22	$M1$	
691.44(5)	6^-	462.914(18)	5^-	228.57(6)[h]	0.087(9)	0.50	$[M1]$	
		317.792(19)	5^-	373.60(6)	0.127(11)	0.13	$[M1]$	
736.39(4)	5^-	588.92(3)	4^-	147.460(19)[h]	0.200(22)	1.71	$[M1]$	
745.47(4)	3^+	658.27(4)	2^+	87.199(8)[d,i]	0.192(14)	7.66	$M1$	
761.49(6)[j]	$(1^-,2^-,3^-)$	322.488(15)	3^-	438.89(7)	0.158(16)	0.09	**[*M1* or *E2*]**	
		210.722(10)	2^-	551.12(9)[a]	0.15(5)	0.05	**[*M1*]**	
		0.0	1^-	760.99(18)[k]	0.207(22)	0.02	**[*M1* or *E2*]**	
785.52(5)[j]		378.535(18)	2^-	406.98(6)	0.197(19)			
796.24(4)[j]	$(\leqslant 3)$	577.87(3)	2^-	218.14(6)[h]	0.114(12)			
		378.535(18)	2^-	418.22(6)[a]	0.23(11)			
		316.531(19)	1^-	479.68(6)	0.63(4)			
		210.722(10)	2^-	584.36(12)[a]	0.16(8)			
		0.0	1^-	796.46(18)[a]	0.18(15)			
819.21(5)[j]	$(2^-,3^-)$	322.488(15)	3^-	496.78(7)	0.37(2)	0.06	**[*M1*]**	
		210.722(10)	2^-	607.50(12)[a]	0.24(9)	0.04	**[*M1*]**	
		174.059(11)	4^-	645.39(9)[a]	0.11(4)	0.03	**[*M1* or *E2*]**	
		59.007(6)	2^-	760.99(18)[k]	0.207(22)	0.02	**[*M1*]**	
821.47(5)[j]	$(\leqslant 3)$	658.27(4)	2^+	163.47(7)[a]	0.13(5)			
		601.82(4)	1^+	219.70(4)	0.237(18)			

TABLE IV. (*Continued.*)

E_i (keV)	$J_i^{\pi_i}$	E_f (keV)	$J_f^{\pi_f}$	E_γ (keV)	σ_γ (b)	α	XL	δ_γ
826.48(5)[j]	(4^-)	686.20(3)	3^-	140.20(5)	0.52(6)	1.12	$E2, M1$	
		588.92(3)	4^-	237.54(17)[a]	0.073(21)	0.45	$[M1]$	
		470.755(21)	3^-	355.84(6)[a]	0.22(5)	0.15	$[M1]$	
855.39(6)[j]	(4^+)	745.47(4)	3^+	109.93(5)	0.157(18)	3.94	$[M1]$	
		658.27(4)	2^+	197.06(12)[a]	0.022(4)	0.34	$[E2]$	
864.70(9)[j]	$(2^-,3^-)$	577.87(3)	2^-	286.83(8)	0.118(11)	0.27	**[*M*1]**	
6179.59(5)	2^+, 3^+	2359.0(5)[i,p]		3820.5(5)[m]	0.018(7)		**(*E*1 or *M*1)**[n]	
		2319.81(23)[i,p]		3859.73(22)[m]	0.068(7)		**(*E*1)**[o]	
		2244.86(15)[j]		3934.68(14)	0.143(11)		**(*E*1)**[o]	
		2219.24(22)[j]		3960.30(21)	0.049(6)		**(*E*1)**[o]	
		2203.4(3)[j]		3976.1(3)	0.049(7)		**(*E*1)**[o]	
		1964.83(14)[j]		4214.71(13)	0.05(3)		**(*E*1)**[o]	
		1905.8(4)[j]		4273.7(4)	0.056(8)		**(*E*1)**[o]	
		1881.39(22)[j]		4298.14(21)	0.172(14)		**(*E*1)**[o]	
		1846.46(22)[j]	$(2^-,3^-)$	4333.07(21)[m]	0.068(9)		**[*E*1]**	
		1838.7(3)[j]	$(1^-,2^-,3^-)$	4340.8(3)[m]	0.046(6)		**[*E*1]**	
		1827.59(17)[j]	$(2^-,3^-,4^-)$	4351.94(16)[m]	0.188(14)		**[*E*1]**	
		1758.0(4)[j]	$(2^-,3^-)$	4421.5(4)[m]	0.090(15)		**[*E*1]**	
		1743.21(22)[j,p]		4436.32(21)[m]	0.104(9)		**(*E*1)**[o]	
		1718.96(24)[j]	$(2^-,3^-,4^-)$	4460.57(23)[m]	0.218(17)		**[*E*1]**	
		1694.7(4)[j,p]	$(2^-,3^-)$	4484.8(4)[m]	0.031(6)		**[*E*1]**	
		1672.3(3)[j]	$(1^-,2^-,3^-)$	4507.2(3)	0.205(15)		**[*E*1]**	
		1659.18(15)[j,p]	$(^-)$	4520.35(14)[m]	0.043(16)		**(*E*1)**[o]	
		1646.93(23)[j]	$(2^-,3^-,4^-)$	4532.60(22)	0.149(16)		**[*E*1]**	
		1628.24(22)[j]	$(2^-,3^-,4^-)$	4551.29(21)	0.080(8)		**[*E*1]**	
		1607.16(22)[j]		4572.37(21)	0.138(11)		**(*E*1)**[o]	
		1601.7(3)[j,p]		4577.8(3)[m]	0.040(6)		**(*E*1)**[o]	
		1587.11(16)[j,p]		4592.42(15)	0.189(13)		**(*E*1)**[o]	
		1572.04(20)[j]	$(1^-,2^-,3^-)$	4607.49(19)[m]	0.086(8)		**[*E*1]**	
		1566.41(18)[j]	$(2^-,3^-,4^-)$	4613.12(17)	0.137(11)		**[*E*1]**	
		1550.71(20)[j]	$(1^-,2^-,3^-)$	4628.82(19)[m]	0.090(7)		**[*E*1]**	
		1545.01(17)[j]	$(^-)$	4634.52(16)	0.312(19)		**(*E*1)**[o]	
		1525.30(20)[j]	(4^-)	4654.23(19)[m]	0.063(6)		**[*E*1]**	
		1486.71(17)[j,p]		4692.81(16)	0.182(13)		**(*E*1)**[o]	
		1475.9(3)[j]	$(^-)$	4703.6(3)	0.110(12)		**(*E*1)**[o]	
		1462.4(5)[j]	$(2^-,3^-)$	4717.1(5)[m]	0.021(5)		**[*E*1]**	
		1457.50(21)[j]	$(2^-,3^-)$	4722.02(20)[m]	0.060(7)		**[*E*1]**	
		1449.8(4)[j]	$(1^-,2^-,3^-)$	4729.7(4)[m]	0.025(5)		**[*E*1]**	
		1437.76(24)[j]		4741.76(23)	0.098(11)		**(*E*1)**[o]	
		1419.0(3)[j]	$(2^-,3^-)$	4760.5(3)[m]	0.053(7)		**[*E*1]**	
		1405.48(16)[j]	$(2^-,3^-,4^-)$	4774.04(15)	0.74(4)		**[*E*1]**	
		1393.0(3)[j]	$(2^-,3^-)$	4786.5(3)[m]	0.032(8)		**[*E*1]**	
		1375.7(7)[j]	$(1^-,2^-,3^-)$	4803.8(7)[m]	0.022(10)		**[*E*1]**	
		1360.3(4)[j]	$(2^-,3^-,4^-)$	4819.2(4)[m]	0.018(5)		**[*E*1]**	
		1355.4(3)[j]	$(2^-,3^-)$	4824.1(3)[m]	0.033(5)		**[*E*1]**	
		1351.21(19)[j]	(4^-)	4828.31(18)	0.094(9)		**[*E*1]**	
		1342.3(4)[j,p]		4837.2(4)[m]	0.017(4)		**(*E*1 or *M*1)**[n]	
		1321.69(20)[j]	$(2^-,3^-)$	4857.83(19)[m]	0.251(17)		**[*E*1]**	
		1317.37(17)[j]	$(2^-,3^-,4^-)$	4862.15(16)	0.71(4)		**[*E*1]**	
		1285.9(9)[j]	$(2^-,3^-)$	4893.7(9)	0.056(9)		**[*E*1]**	
		1242.70(21)[j]	$(2^-,3^-)$	4936.82(20)[m]	0.35(3)		**[*E*1]**	

TABLE IV. (*Continued.*)

E_i (keV)	$J_i^{\pi_i}$	E_f (keV)	$J_f^{\pi_f}$	E_γ (keV)	σ_γ (b)	α	XL	δ_γ
6179.59(5)	$2^+, 3^+$	1240.3(3)[j,p]		4939.2(3)[m]	0.079(16)		**(*E*1)**[o]	
		1231.3(3)[j]	$(2^-,3^-)$	4948.2(3)[m]	0.058(6)		**[*E*1]**	
		1227.94(21)[j,p]		4951.58(20)[m]	0.138(10)		**(*E*1)**[o]	
		1212.0(4)[j,p]		4967.5(4)[m]	0.023(5)		**(*E*1 or *M*1)**[n]	
		1197.95(18)[j]	$(2^-,3^-)$	4981.57(17)	0.315(20)		**[*E*1]**	
		1185.05(19)[j]	$(2^-,3^-)$	4994.47(18)	0.115(9)		**[*E*1]**	
		1172.25(18)[j]	$(^-)$	5007.27(17)	0.91(5)		**(*E*1)**[o]	
		1157.85(20)[j]	$(2^-,3^-,4^-)$	5021.66(19)[m]	0.099(8)		**[*E*1]**	
		1151.19(18)[j]	(4^-)	5028.32(17)	0.86(5)		**[*E*1]**	
		1140.9(3)[j]	$(2^-,3^-)$	5038.6(3)[m]	0.028(4)		**[*E*1]**	
		1132.12(20)[j]		5047.39(19)	0.104(8)		**(*E*1)**[o]	
		1122.55(23)[j]	$(2^-,3^-)$	5056.96(22)[m]	0.083(8)		**[*E*1]**	
		1102.74(18)[j]	$(2^-,3^-)$	5076.77(17)[m]	0.262(17)		**[*E*1]**	
		1097.06(18)[j]	(4^-)	5082.45(17)	0.173(11)		**[*E*1]**	
		1071.5(6)[j,p]	$(2^-,3^-)$	5108.0(6)[m]	0.025(8)		**[*E*1]**	
		1068.61(22)[j]	$(2^-,3^-)$	5110.90(21)	0.148(12)		**[*E*1]**	
		1057.5(5)[j]	$(2^-,3^-)$	5122.0(5)[m]	0.013(4)		**[*E*1]**	
		1053.8(6)[j]	$(1^-,2^-,3^-)$	5125.7(6)[m]	0.012(4)		**[*E*1]**	
		1040.30(19)[j]	$(2^-,3^-,4^-)$	5139.21(18)	0.78(5)		**[*E*1]**	
		1017.65(17)[j,p]	$(2^-,3^-,4^-)$	5161.86(16)[m]	0.010(3)		**[*E*1]**	
		1013.7(3)[j]	$(2^-,3^-,4^-)$	5165.74(24)[m]	0.043(4)		**[*E*1]**	
		1003.08(19)[j,p]	$(2^-,3^-,4^-)$	5176.43(18)	0.50(3)		**[*E*1]**	
		988.97(22)[j]	$(2^-,3^-)$	5190.54(21)[m]	0.051(6)		**[*E*1]**	
		982.32(18)[j,p]		5197.19(17)[m]	0.050(5)		**(*E*1)**[o]	
		973.31(20)[j]	$(^-)$	5206.20(19)	0.275(18)		**(*E*1)**[o]	
		954.78(23)[j]		5224.73(22)	0.048(5)		**(*E*1)**[o]	
		935.37(20)[j]	$(2^-,3^-)$	5244.14(19)	0.128(9)		**[*E*1]**	
		923.57(20)[j]	$(2^-,3^-)$	5255.94(19)	0.307(19)		**[*E*1]**	
		902.43(19)[j]	$(2^-,3^-)$	5277.08(18)	0.46(3)		**[*E*1]**	
		895.15(19)[j]	$(2^-,3^-,4^-)$	5284.36(18)[m]	0.230(15)		**[*E*1]**	
		888.70(24)[j]	(4^-)	5290.81(23)	0.040(5)		**[*E*1]**	
		856.3(5)[j]	$(2^-,3^-)$	5323.2(5)[m]	0.013(3)		**[*E*1]**	
		826.48(5)[j]	(4^-)	5353.09(20)	0.46(3)		**[*E*1]**	
		819.21(5)[j]	$(2^-,3^-)$	5360.18(20)	0.214(13)		**[*E*1]**	
		796.24(4)[j]	$(\leqslant 3)$	5383.06(19)	0.086(6)		**(*E*1)**[o]	
		791.3(3)[j]	(1^-)	5388.19(24)[m]	0.035(4)		**[*E*1]**	
		761.49(6)[j]	$(1^-,2^-,3^-)$	5418.6(3)[m]	0.0142(23)		**[*E*1]**	
		753.50(22)[j]	$(2^-,3^-)$	5426.00(21)[m]	0.035(3)		**[*E*1]**	
		686.20(3)	3^-	5493.50(18)	0.297(18)		**[*E*1]**	
		680.21(4)	**2^-**	5499.4(3)[m]	0.031(3)		**[*E*1]**	
		623.97(5)	1^-	5555.4(8)[m]	0.0065(23)		**[*E*1]**	
		577.87(3)	2^-	5601.65(18)	0.367(22)		**[*E*1]**	
		534.32(5)	4^-	5645.07(20)	0.257(16)		**[*E*1]**	
		469.945(19)	4^-	5709.67(20)	0.386(24)		**[*E*1]**	
		425.70(3)	**4^+**	5753.2(3)[m]	0.024(4)		**[*M*1]**	
		420.51(3)	4^+	5759.1(8)	0.006(3)		**[*M*1]**	
		378.535(18)	2^-	5800.93(21)	0.051(4)		**[*E*1]**	
		322.488(15)	3^-	5856.95(19)	0.46(3)		**[*E*1]**	
		316.531(19)	1^-	5863.4(3)[m]	0.040(3)		**[*E*1]**	
		273.566(12)	4^-	5905.7(2)[m]	0.095(9)		**[*E*1]**	
		268.729(12)	4^-	5910.62(19)	2.00(5)		**[*E*1]**	

TABLE IV. (*Continued.*)

E_i (keV)	$J_i^{\pi_i}$	E_f (keV)	$J_f^{\pi_f}$	E_γ (keV)	σ_γ (b)	α	XL	δ_γ
6179.59(5)	$2^+, 3^+$	210.722(10)	2^-	5968.92(24)	0.052(4)		**[*E*1]**	
		174.059(11)	4^-	6005.59(21)	0.184(12)		**[*E*1]**	
		146.227(9)	3^-	6033.26(21)	0.250(15)		**[*E*1]**	
		99.381(7)	3^-	6080.29(20)	0.406(24)		**[*E*1]**	
		59.007(6)	2^-	6120.38(20)	0.397(23)		**[*E*1]**	
		0.0	1^-	6179.30(21)	0.059(4)		**[*E*1]**	

[a]Multiplet resolved using ENSDF branching ratios [10].
[b]Multiplet resolved using x-ray yields from Ref. [24].
[c]Multiplet resolved using statistical-model calculations.
[d]Transition not observed; γ-ray energy taken as ENSDF value [10] or deduced from level-energy difference.
[e]Transition not observed; intensity deduced from ENSDF branching ratios [10].
[f]Level energy from Ref. [56].
[g]Multiplet resolved using γ-ray branching ratio adjusted to optimize agreement with statistical-model calculations.
[h]γ-ray multiply-placed in level scheme; intensity divided using statistical-model calculations.
[i]Transition not observed; intensity deduced from statistical-model calculations.
[j]Level above E_c not included in statistical-model calculations.
[k]γ-ray multiply-placed in level scheme; undivided intensity given.
[l]Mixing ratio other than the mean or limiting value from the ENSDF [10] used to calculate α.
[m]Newly identified primary γ-ray transition not found in literature.
[n]Primary γ ray with $\sigma_\gamma < 0.03$ b assigned tentative $E1$ or $M1$ multipolarity.
[o]Primary γ ray with $\sigma_\gamma \geqslant 0.03$ b assigned tentative $E1$ multipolarity.
[p]Level proposed in Ref. [55].

levels from Refs. [10,55]. γ rays were placed in the ^{186}Re level scheme by matching the fitted peak energies from the prompt γ-ray spectrum with the energies of known transitions in the ENSDF [10]. Due to the high level density of ^{186}Re, peaks in the singles γ-ray spectra were often convolved in multiplets, which made direct measurement of the γ-ray intensities difficult. In these cases, identified by footnotes in Table IV, statistical-model calculations (for γ rays deexciting levels below $E_c = 746$ keV) or branching ratios from the ENSDF [10] were used to normalize the cross sections.

Production cross sections for multiply-placed γ rays for which the ENSDF provides only the undivided intensity [10], identified by footnotes in Table IV, were determined by dividing the total γ-ray intensity as necessary to optimize agreement between the level population from the statistical model and the experimental depopulation ($\sum_i \sigma_{\gamma_i}(1+\alpha_i)/\sigma_0$; where the summation is over all γ rays depopulating a given level). For the 218.1-, 228.6-, 193.8-, and 469.4-keV γ rays deexciting the 317.8-, 646.3-, 691.4-, and 785.5-keV levels, respectively [10], the intensity resulting from this procedure was sufficiently small that there was no strong evidence for the existence of these γ rays on the basis of statistical-model results. These four γ rays are omitted from Table IV. The highly-internally converted ($\alpha \approx 4.1 \times 10^6$) 50-keV γ ray [10] deexciting the 148.2-keV, $J^\pi = (8^+)$ isomer [56], and the 142.8-keV γ ray reported in the ENSDF as deexciting the 997.8-keV level [10] were not observed in the prompt γ-ray spectrum and are also omitted from Table IV.

Level spin-parity (J^π) assignments, transition multipolarities (XL) and multipole mixing ratios (δ_γ) in Table IV were taken from the ENSDF [10] when available, while internal-conversion coefficients (α) were calculated with BRICC [36]. Unknown transition multipolarities between levels with definite J^π assignments were assumed to be the lowest multipole order permitted by angular-momentum selection rules. It is important to note that many of these transitions may have mixed-multipole character, but the effect of multipole mixing on internal-conversion-corrected γ-ray production cross sections used in the statistical model is negligible for higher-energy ($E_\gamma > 250$ keV) transitions. For lower-energy ($E_\gamma \leqslant 250$ keV) γ-ray transitions, level populations calculated using the statistical model can be used to estimate multipole mixing ratios, discussed later in the text.

Transitions with $E_\gamma \gtrsim 3.5$ MeV were assumed to be primary γ-ray transitions, and were identified as such in Table IV provided they satisfied the following criterion for a known level with excitation energy E_f:

$$S_n = E_\gamma + E_f + E_r. \tag{21}$$

Here S_n is the neutron-separation energy, E_γ is the measured γ-ray energy, and $E_r = E_\gamma^2/2A$ is the recoil energy of the nucleus (A is the atomic mass of the product nucleus). Of the primary transitions identified in this way, 50 were not previously reported in the evaluated literature (Refs. [57–60]). Of these 50 new primary transitions, 35 feed levels in the adopted level scheme for ^{186}Re [10]. The remaining 15 primary γ rays feed levels reported by Wheldon *et al.* in Ref. [55], in which levels in ^{186}Re were populated by (p,d) reactions on ^{187}Re at proton energies of 21 MeV. New primary γ rays are identified by footnotes in Table IV, with multipolarity assignments estimated on the basis of observed γ-ray intensities relative to the intensities of primary transitions with known multipolarity. The highest-intensity primary transition with $M1$ multipolarity (assumed from angular momentum selection rules), has an

intensity of $\sigma_\gamma = 0.024(4)$ b, so primary transitions with $\sigma_\gamma \geqslant 0.03$ b that feed levels without a definite J^π assignment are given tentative multipolarities of $E1$, or tentative $E1$ or $M1$ multipolarity if $\sigma_\gamma < 0.03$ b.

A. Nuclear structure

The predicted population of individual low-lying levels from statistical-model calculations can be plotted against the experimental depopulation, hereafter referred to as a population-depopulation (P-D) plot. Good agreement between the values, indicated by a line of slope 1 in the P-D plot and residual differences of less than 3 standard deviations (σ), provides support for the choice of LD and PSF models used, the placement of transitions and spin-parity assignments for levels below E_c in the level scheme, γ-ray branching ratios, and multipole mixing ratios δ_γ. This comparison can be used as an effective tool for evaluating the completeness and accuracy of the decay scheme. Preempting the results presented later in this section, optimal agreement in the P-D plot is achieved with the MGLO ($k_0 = 2.9$) model for the PSF (assuming the parametrization of Ref. [49]) and the CTF LD model (assuming the parametrization of Ref. [40]). The resulting P-D plot, which was generated for a critical energy of $E_c = 746$ keV and with the level spin-parity assignments, branching ratios, and multipole mixing ratios discussed later in the text, is shown in Fig. 6.

1. Capture-state spin composition

The ground-state spin-parity of the target nucleus ^{185}Re is $J^\pi_{\text{g.s.}} = 5/2^+$ [61], so s-wave neutron capture results in a ^{186}Re compound nucleus with an admixture of 2^+ and 3^+ spins. The total experimental capture cross section σ_0 is equal to the sum of the cross sections $\sigma(+,-)$ for populating the low-spin (2^+) and high-spin (3^+) resonances, and the cross section $\sigma(B)$ for populating any bound resonances (with spin $J_{\text{g.s.}} \pm 1/2$), according to the expression

$$\sigma_0 = \sigma_\gamma(-) + \sigma_\gamma(+) + \sigma_\gamma(\text{B}). \tag{22}$$

There is one bound resonance with an energy of -4.466 eV relative to the neutron-separation energy of ^{186}Re, which has a tentative spin assignment of $J = (3)$ listed in Ref. [35]. The expression in Eq. (22) implies a capture-state spin composition with a fraction F^- in the low-spin 2^+ state given by

$$F^- = \frac{\sigma(-)}{\sigma_0}. \tag{23}$$

Using values of $\sigma_\gamma(+) = 58.9$ b for populating the $J^\pi = 3^+$ state, $\sigma_\gamma(-) = 1.3$ b for populating the $J^\pi = 2^+$ state, and $\sigma_\gamma(\text{B}) = 51.8$ b from Ref. [35], the resulting fraction is $F^- = 0.012$. Given the tentative nature of the $J = (3)$ spin assignment for the bound resonance, an alternative possibility is that the bound resonance has spin $J = 2$, which would result in a fraction

$$F^- = \frac{\sigma(-) + \sigma(\text{B})}{\sigma_0} \tag{24}$$

in the 2^+ state, equal to $F^- = 0.474$ using the cross sections from Ref. [35]. Statistical-model calculations were performed using both capture-state spin compositions, and the best agreement between modeled population and experimental depopulation is consistently achieved with $F^- = 0.012$. This composition is adopted for all calculations described in this work, and our results support the tentative claim of a $J = (3)$ assignment for the bound resonance [35].

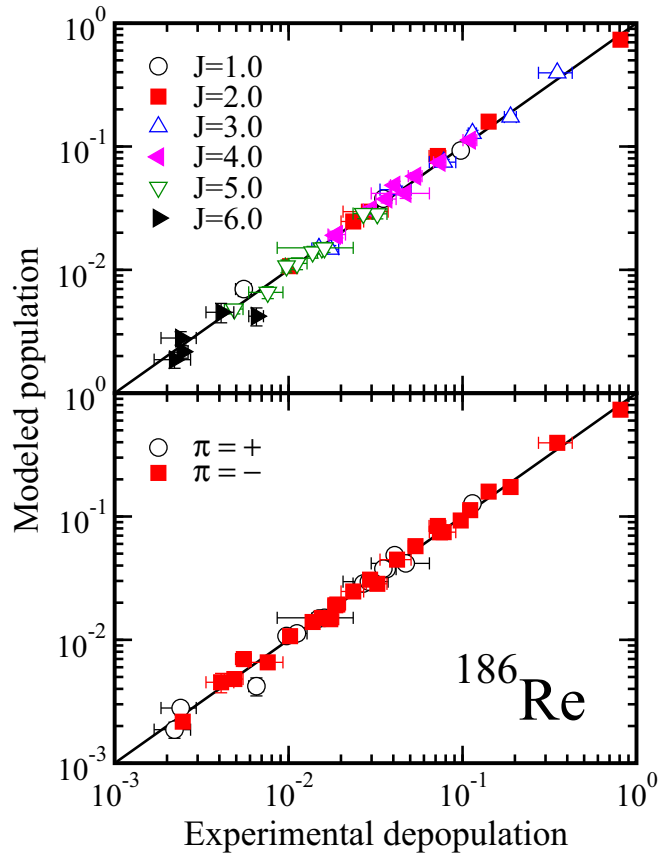

FIG. 6. Plot of modeled population versus experimental depopulation (P-D plot) resulting from statistical-model calculations with a critical energy of $E_c = 746$ keV, using the MGLO model with $k_0 = 2.9$ for the PSF and the CTF model for the LD with the parametrization described in Ref. [40]. The calculations used to generate this plot assume the level J^π assignments summarized in Table V and the branching ratio and multipole-mixing ratio adjustments described in the text.

2. Discrete-level spin-parity assignments

The spin and parity is known unambiguously only for the ground state of ^{186}Re [10]. All excited states have only tentative assignments in the adopted level scheme [10]. The simulated population of low-lying levels depends on their J^π assignments, and the population of specific levels is largely independent of the choices of LD and PSF models. Therefore, a population-depopulation comparison provides a means of checking tentative J^π assignments for individual levels. Using the statistical model, we were able to confirm tentative assignments or suggest new values based on optimal agreement with experimental data (revealed through P-D plots) for all states below $E_c = 746$ keV in ^{186}Re. In this work, we

TABLE V. Level J^π assignments from the ENSDF adopted level scheme [10] and the proposed assignments from this work, based on observed agreement between experimental depopulation and modeled population. Levels are arranged according to their excitation energy E_x.

E_x (keV)	J^π_{ENSDF}	$J^\pi_{\text{this work}}$
351.25(3)	$(3)^+$	4^+
425.70(3)	$(2^+,3^+,4^+)$	4^+
~471	$(4)^+$	6^+
500.74(6)	$(4)^+$	5^+
549.16(5)	$(^+)$	5^+
665.23(6)	$(5)^+$	6^+
680.21(4)	$(2^-,3^-)$	2^-

have confirmed 32 previously tentative J^π assignments and recommend new assignments for seven other levels in ^{186}Re, which are summarized in Table V. This technique of using statistical-decay model agreement with experimental data to propose J^π assignments has been employed previously in Ref. [3].

The improvement in the P-D plots after adjusting the J^π assignments for the 351.3-, ~471-, 500.7-, and 665.2-keV levels is evident from the significant reduction observed in the absolute residual differences $|R|$ between the modeled population and the experimental depopulation for these levels, shown in Fig. 7. Adjusting the J^π assignment of a particular level can affect the feeding to other levels below it in the level scheme, so the proposals listed in Table V also improved agreement in the P-D plots for several other levels, which can be seen in Fig. 7.

The new assignments proposed in this work are discussed, in turn, below.

351.3-, 500.7-, and 665.2-keV levels. The 351.3-keV level has a spin-parity assignment of $(3)^+$ in the adopted level scheme [10], based on the existence of an $E1$ transition to the $J^\pi = (3)^-$, 99.4-keV level. The multipolarity of this transition was determined from conversion-electron spectrometry by Lanier *et al.* [58]. Glatz [59] determined the 351.3-keV level to be the $K^\pi = (3)^+$ band head, and placed the $J^\pi = (4)^+$, 500.7-keV and $J^\pi = (5)^+$, 665.2-keV levels in the rotational band according to $\gamma - \gamma$ coincidences from (n,γ) reactions on ^{185}Re. In this work, agreement in the P-D plot for the 351.3-keV level is significantly improved when the spin is increased to $J = 4$, as illustrated in Fig. 7. A $J^\pi = 4^+$ assignment for the 351.3-keV level remains consistent with the measured $E1$ multipolarity for the 251.9-keV transition to the 99.4-keV level. For the first member of the rotational band built on the 351.3-keV band head, the agreement between the modeled population and experimental depopulation is improved when the assignment for the 500.7-keV level is changed to $J^\pi = 5^+$. The rotational band structure implies an assignment of $J^\pi = 6^+$ for the 665.2-keV level. Unfortunately the 164.5-keV transition deexciting this level is part of a multiplet, and its intensity was adjusted using the DICEBOX results, so the P-D plots before and after the spin adjustment could not be compared.

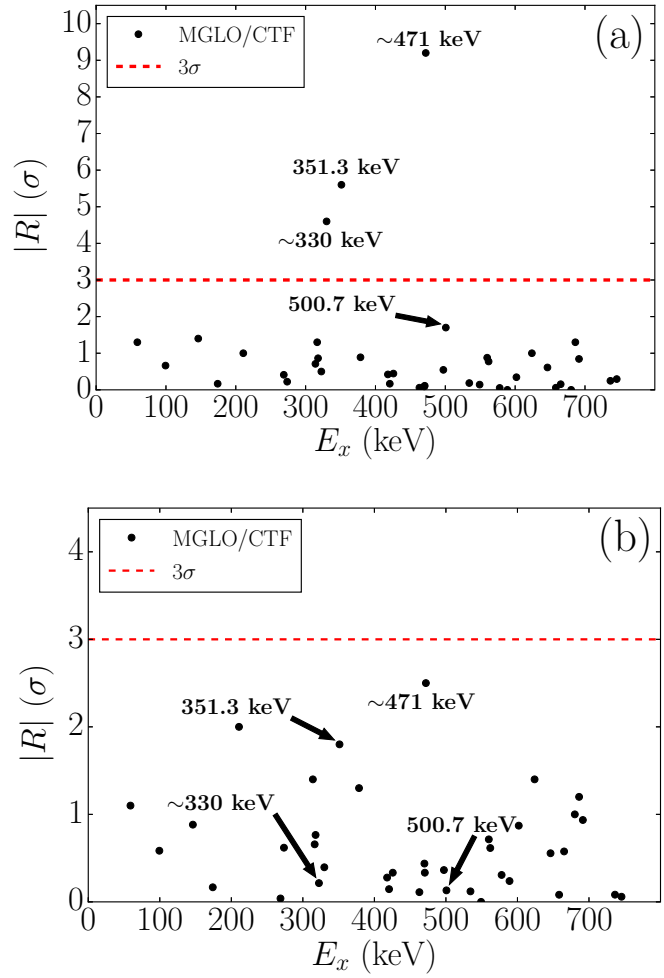

FIG. 7. Plots of the absolute value of the residual difference $|R|$, in units of standard deviations σ, between the modeled population and experimental depopulation as a function of level excitation energy E_x, for (a) levels before spin-parity adjustments, (b) after the spin-parity assignments for the 351.3-, ~471-, 500.7-, and 665.2-keV levels are adjusted as described in the text. The ~330-keV level is highlighted because its population is influenced by the J^π assignment of the ~471-keV level that directly feeds it. In both panels, the assignments for the 425.7-, 549.2-, and 680.2-keV levels are taken to be the proposed values from Table V. The horizontal dashed line identifies a residual difference of 3σ. Both plots result from statistical-model calculations using the MGLO model with $k_0 = 2.9$ for the PSF and the CTF model for the LD with the parametrization described in Ref. [40].

425.7-keV level. This level has an indefinite spin-parity assignment of $J^\pi = (2^+,3^+,4^+)$ in the adopted level scheme [10], deduced from the existence of a 111.7-keV transition that feeds the $J^\pi = (3)^+$ level at 314.0 keV. Of the three suggested values for the 425.7-keV level, the $J^\pi = 4^+$ assignment provides optimal agreement between the modeled population and the experimental depopulation for both the 425.7- and 314.0-keV levels.

~471-keV level. The $J^\pi = (4)^+$ assignment in the ENSDF [10] for this level is based on a tentative $(\pi 9/2^-[514]) - (\nu 1/2^-[510])$ configuration from Ref. [59] and

the existence of a mixed $M1+E2$ transition feeding the $J^\pi = (5)^+$ level at ~330-keV. Calculations assuming the adopted spin-parity assignment for the ~471-keV level produce a significantly greater population than the experimentally observed depopulation for both the ~330-keV level and the ~471-keV level, which is clear from Fig. 7(a). Optimal agreement in the P-D plot for both of these levels is achieved with a $J^\pi = 6^+$ assignment for the ~471-keV level [Fig. 7(b)], and this assignment is consistent with a transition to the $J^\pi = (5)^+$, ~330-keV level with mixed $M1+E2$ multipolarity. The $J^\pi = 6^+$ assignment proposed in this work may suggest that the ~471-keV level is the first member of a rotational band built on the $K^\pi = (5)^+$, ~330 -keV level.

549.2-keV level. No spin assignment for this level is provided in the adopted level scheme [10], and it has only a tentative $\pi = (+)$ parity assignment based on the existence of a 123.5 -keV $M1(+E2)$ transition feeding the 425.7 -keV level from (n,γ) and (d,p) measurements by Lanier *et al.* [58]. Assuming a $J^\pi = 4^+$ assignment for the 425.7 -keV level as discussed above, the possible assignments for the 549.2 -keV level that are consistent with the measured $M1(+E2)$ multipolarity for the transition to the 425.7 -keV level are $J^\pi = 3^+$, 4^+, and 5^+. Of these, the $J^\pi = 5^+$ assignment produces the best agreement in the resulting P-D plot.

680.2-keV level. In the adopted level scheme, this level has an indefinite spin-parity assignment of $J^\pi = (2^-,3^-)$ [10] due to the existence of γ rays feeding the $J^\pi = 1^-$ ground state, the $J^\pi = (2)^-$ level at 210.7 keV, and the $J^\pi = (3)^-$ state at 322.5 keV. A $J^\pi = 2^-$ assignment results in the best agreement between the modeled level population and the experimental depopulation, and implies the three γ-ray transitions deexciting this level have some degree of $M1$ character.

3. *Isomer feeding, multipole mixing, and branching ratios*

Four other levels below E_c also warrant discussion here:

148.2-keV level. The $J^\pi = (8^+)$ isomer, recently reported in Ref. [56] to have an excitation energy of 148.2(5) keV (cf. the adopted value of 149(7) keV [10]), is very weakly populated due to its large spin difference from the capture state. There was no observation of the highly converted 50-keV transition deexciting the level [10] in the prompt γ-ray spectrum. As a result, no P-D comparison could be made. Calculations that include this level result in a cross section for populating the isomer equal to 0.071(24) b. Two measurements have been made of the ratio of thermal-neutron capture cross sections for the ^{185}Re$(n,\gamma)^{186}$Re^m and ^{185}Re$(n,\gamma)^{186}$Re^g reactions using activation techniques: 0.3% [57] and 0.54(11)% [62]. When combined with the adopted value of $\sigma_0 = 112(2)$ b for populating the ^{186}Re ground state [35], these ratios yield isomer cross sections of 0.34(10) b and 0.60(12) b, respectively. The discrepancy between the measured and calculated cross sections for isomer population may imply there are levels or transitions missing from the adopted level scheme below E_c that feed the isomer. A recent investigation of ^{187}Re$(n,2n)$ reactions by Matters *et al.* reported two feeding levels at 414.9 keV and 796.1 keV [56], but because these levels have proposed spin-parity assignments of $J^\pi = (9^+)$ and (10^+) they are also weakly populated in the (n,γ) reaction, and their inclusion in the calculations does not correct the discrepancy. Given the $J^\pi = 6^+$ assignment proposed above for the ~471-keV level, it is possible that this level feeds the isomer via an unplaced $E2$ transition with an energy of ~323-keV. In the prompt γ-ray spectrum, there are three such unplaced γ rays at 321.57(7) keV, 322.61(9) keV, and 323.99(7) keV, with partial cross sections of 0.234(24) b, 0.204(21) b, and 0.143(14) b, respectively, which could partly account for the discrepancy. Isomer feeding from the $J^\pi = (6)^-$, ~186-keV level, discussed below, is another possibility. These hypotheses could not be verified in this study, because no γ-γ coincidence data was collected.

~186-keV level. The $J^\pi = (6)^-$, ~186-keV level is directly fed by the $J^\pi = (5)^+$, ~330-keV level via an $E1$ transition, and has a modeled population of 4.5(4) b. In the adopted level scheme for ^{186}Re, there are no transitions out of this level to lower-lying levels [10], although a ~12-keV $E2$ transition to the $J^\pi = 4^-$, 174.1-keV level and a ~38-keV $M2$ transition to the 148.2-keV isomer have been proposed in the literature (Refs. [58], [57], and [59]). Both transitions would be highly converted ($\alpha = 7.1 \times 10^4$ for the ~12-keV transition and $\alpha = 1.0 \times 10^3$ for the ~38-keV transition), and their energies would be sufficiently low that they would not be observable in the prompt ^{185}Re(n,γ) spectrum of this work. The modeled population of the ~186-keV level gives an upper bound for the γ-ray cross section of each of these two possible transitions, which are listed in Table IV. It should be noted that the modeled population and experimental depopulation of the 174.1-keV level is balanced prior to including the ~12-keV transition in the calculations, but the mixed $M1+E2$, 74.7-keV γ ray deexciting this level is part of a multiplet and its cross section was normalized using the statistical model. In this work, the ENSDF value of $\delta_\gamma = 0.19(6)$ [10] for the multipole-mixing ratio (adopted on the basis of subshell ratios from Ref. [58]) was used to arrive at a conversion coefficient of $\alpha = 11.96$ for this transition. Another value for the mixing ratio, $\delta_\gamma = 0.9(2)$, has been proposed [10] based on the value of $\alpha_{L1} = 0.93(13)$ from Ref. [58], which would result in a conversion coefficient of $\alpha = 12.82$ and further increase the depopulation of the 174.1-keV level. Finally, the possibility of an unobserved 27.8-keV $M1$ transition from the 174.1-keV level to the $J^\pi = 3^-$, 146.2-keV level suggests that the agreement in the P-D plot for the 174.1-keV level could be maintained with the inclusion of significant feeding from the ~186-keV level.

378.5-keV level. For most levels, optimum agreement in the P-D plot is obtained when the mean or limiting values of the experimentally-measured multipole-mixing ratios [10] are used to compute internal conversion coefficients. In cases where adjusting the mixing ratio (within the limits of the uncertainty in the adopted value) significantly improves the agreement between the modeled population and the experimental depopulation, statistical-model calculations may be used to infer better values for the mixing ratios. For the 62.2-keV transition from the 378.5-keV level to the 316.5-keV level, the multipolarity from the ENSDF is given as $M1(+E2)$, with an upper bound on the mixing ratio of $\delta_\gamma \leqslant 1.0$ [10]. Statistical-model results suggest that transition has pure $M1$

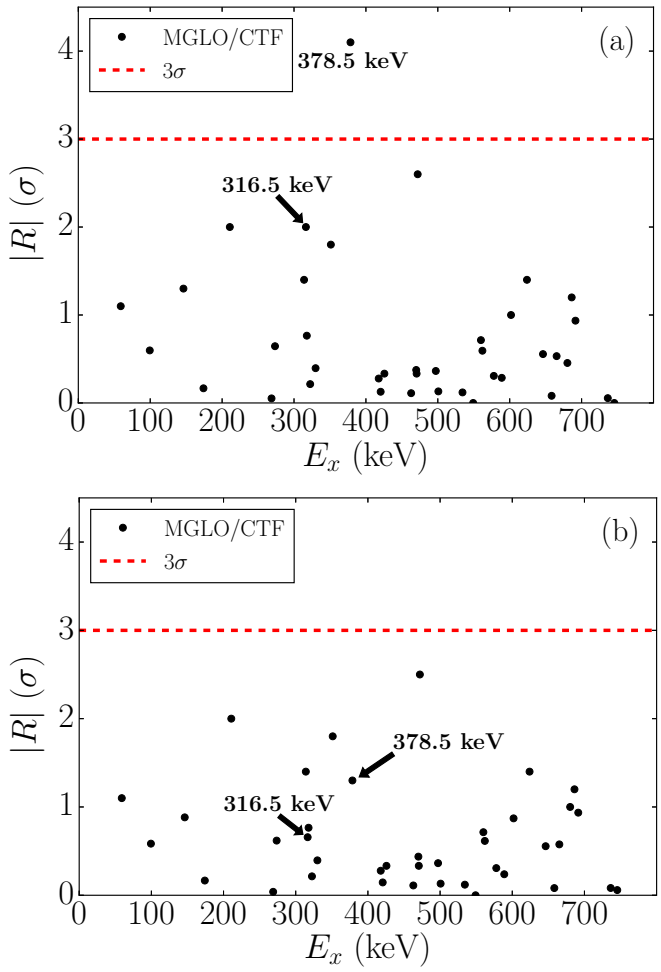

FIG. 8. Plots of the absolute value of the residual difference $|R|$, in units of standard deviations σ, between the modeled population and experimental depopulation as a function of level excitation energy E_x, assuming (a) mixed $M1+E2$ character for the 62.2-keV transition deexciting the 378.5-keV level with a mixing ratio of $\delta_\gamma = 1.0$ [10], and (b) pure $M1$ character ($\delta_\gamma = 0$) for this transition. The horizontal dashed line identifies a residual difference of 3σ. Both plots result from statistical-model calculations with the J^π assignments from Table V assumed, using the MGLO model with $k_0 = 2.9$ for the PSF and the CTF model for the LD with the parametrization described in Ref. [40].

multipolarity, because a mixing ratio of $\delta_\gamma = 0$ optimizes agreement in the P-D plot for the 378.5-keV level while simultaneously improving agreement for the 316.5-keV level. This improvement is evident from the residuals plots shown in Fig. 8.

534.3-keV level. The ENSDF branching ratio for the 259.8-keV γ ray deexciting the 534.3-keV level is quoted as $I_\gamma = 31$ (with no stated uncertainty) relative to the intensity of $I_\gamma = 100(15)$ for the 360.5-keV γ ray deexciting the same level [10]. The branching ratios in the ENSDF for the 534.3-keV level were determined from the work of Lanier *et al.*, in which prompt γ-ray spectra from (n,γ) reactions on ^{185}Re were measured using a bent-crystal spectrometer [58], and are not reported elsewhere in the literature. The 259.8-keV γ ray is part of a multiplet, and normalizing its partial cross section to that of the 360.5-keV γ ray using the ENSDF branching ratios results in a modeled population that exceeds the experimental depopulation by a residual difference of 3.5σ. The 534.3-keV level is fed by a relatively strong $E1$ primary transition with $E_\gamma = 5645.07(20)$ keV, so increasing the spin from its adopted assignment of $J^\pi = (4)^-$ to improve agreement in the P-D plot is not possible. Agreement between the modeled population and experimental depopulation for the 534.3-keV level, as well as the 378.5-keV level fed by the 259.8-keV γ ray, is optimized when the branching ratio is adjusted to $I_\gamma = 80(10)$ relative to the intensity of the 360.5-keV γ ray stated above. On the basis of the observed improvement in the P-D plot, we assess that the branching ratios in the ENSDF for this level may be incorrect, and we have adopted the revised value of the relative intensity, $I_\gamma = 80(10)$, for statistical-model calculations in this work. A possible alternative explanation for the lack of agreement observed in the P-D plot could be an unplaced γ ray that deexcites the 534.3-keV level.

B. Total radiative thermal-neutron capture cross section for ^{185}Re(n,γ)

After arriving at a list of partial γ-ray production cross sections σ_γ and making the adjustments to the level scheme described above, DICEBOX was used to compute the fraction P_0 of the total capture cross section σ_0 resulting from ground-state feeding from the quasicontinuum. The sum of the internal-conversion-corrected experimental cross sections $\sum_i \sigma^{\rm exp}_{\gamma i0}(1+\alpha_i)$ for feeding the ground state from levels below $E_c = 746$ keV was used with the calculated value of P_0 in Eq. (20) to calculate a total ^{185}Re(n,γ) thermal-neutron capture cross section σ_0 for a variety of PSF and LD model combinations. The agreement between the calculated mean s-wave resonance radiative width Γ_0 and the adopted value of $\langle\Gamma_0\rangle = 56(3)$ meV [35] was also used to assess the choices of LD and PSF models and parameters used in the calculations. The results of these calculations are shown in Table VI.

It is evident from Table VI that the particular choices of PSF and LD models and LD parametrization used do not produce statistically significant changes in the value of σ_0, which permits the determination of a model-independent value for σ_0. However, the s-wave resonance radiative width Γ_0 is relatively sensitive to the choices of PSF and LD models. This observed sensitivity in the calculated value of Γ_0 to the choice of models has been observed previously in studies involving the tungsten [3,7] and palladium [4] isotopes. The best agreement in the P-D plots was consistently achieved with the MGLO/CTF combination of PSF/LD models, using the LD parametrization from Ref. [40], while the KMF/BSFG model combination with the LD parameters from Ref. [40] most accurately reproduced the literature value of Γ_0. We tested parity-dependent as well as parity-independent LD models in this work, and the results for these two options are fully consistent. The values for P_0 from Table VI were used to obtain a model-independent total radiative thermal-neutron capture cross section of $\sigma_0 = 111(6)$ b, which is in perfect agreement with the adopted value of $\sigma_0 = 112(2)$ b from Ref. [35]. This

TABLE VI. Total radiative thermal-neutron capture cross sections (σ_0), simulated fractions of transitions from the quasicontinuum to the ground state (P_0), and mean s-wave resonance radiative widths (Γ_0), corresponding to various combinations of $E1$ PSF and LD models and LD parametrizations. Fluctuations in Γ_0 and P_0, which lead to the uncertainties in the tabulated values, result from different nuclear realizations. For each combination, the sum of the internal-conversion-corrected experimentally measured cross sections from levels below $E_c = 746$ keV directly to the ground state is $\sum_i \sigma_{\gamma i0}^{\exp}(1+\alpha_i) = 106.8(57)$ b.

PSF/LD	P_0	σ_0 (b)	Γ_0 (meV)
MGLO/CTF[a]	0.0400(59)	111.2(60)	43.8(9)
MGLO/CTF[b]	0.0380(57)	111.0(59)	39.6(7)
MGLO/BSFG[a]	0.0366(51)	110.9(59)	78.6(9)
MGLO/BSFG[b]	0.0337(50)	110.5(59)	101.8(25)
GLO/CTF[a]	0.0395(55)	111.2(60)	27.6(4)
GLO/CTF[b]	0.0376(56)	111.0(59)	25.4(3)
GLO/BSFG[a]	0.0360(52)	110.8(59)	48.8(4)
GLO/BSFG[b]	0.0334(42)	110.5(59)	62.6(11)
KMF/CTF[a]	0.0409(61)	111.3(60)	32.7(6)
KMF/CTF[b]	0.0392(53)	111.1(60)	29.4(5)
KMF/BSFG[a]	0.0376(51)	111.0(59)	58.7(6)
KMF/BSFG[b]	0.0342(44)	110.6(59)	74.9(17)
BA/CTF[a]	0.0403(75)	111.3(60)	89.4(23)
BA/CTF[b]	0.0376(66)	111.0(60)	75.1(16)
BA/BSFG[a]	0.0367(60)	110.9(59)	164.5(21)
BA/BSFG[b]	0.0332(65)	110.5(59)	204.4(60)

[a]Assuming the LD parametrization from Ref. [40].
[b]Assuming the LD parametrization from Ref. [41].

value is also statistically consistent with each of the previous cross section measurements listed in Table VII.

The stability in the value of σ_0 as a function of E_c, which is similar to the behavior observed in the tungsten isotopes investigated in Refs. [3,7], is shown in Fig. 9. It is evident from Fig. 9 that the experimental contribution $\sum_i \sigma_{\gamma i0}^{\exp}(1+\alpha_i)$ and σ_0 have converged to a statistically-consistent value by $E_c = 317$ keV, though the study described in this work was extended up to $E_c = 746$ keV to make a more complete assessment of the ^{186}Re level scheme.

TABLE VII. Summary of total thermal-neutron capture cross section (σ_0) measurements on ^{185}Re.

Reference	Method	σ_0 (b)
This work	**PGAA**	**111(6)**
Mughabghab [35]	Evaluation	112(2)
Seren *et al.*[64]	Activation	101(20)
Pomerance [65]	Pile oscillator	100(8)
Lyon [66]	Activation	127.0(127)
Karam *et al.*[67]	Activation	96.5(100)
Friesenhahn *et al.* [68]	Activation	105(10)
Heft [69]	Activation	116(5)
De Corte *et al.*[70]	Activation	112(18)[a]
Hayakawa *et al.*[62]	Activation	132(26)
Farina-Arbocco *et al.*[71]	Activation	111.6(11)

[a]Calculated using I_0 from Ref. [35].

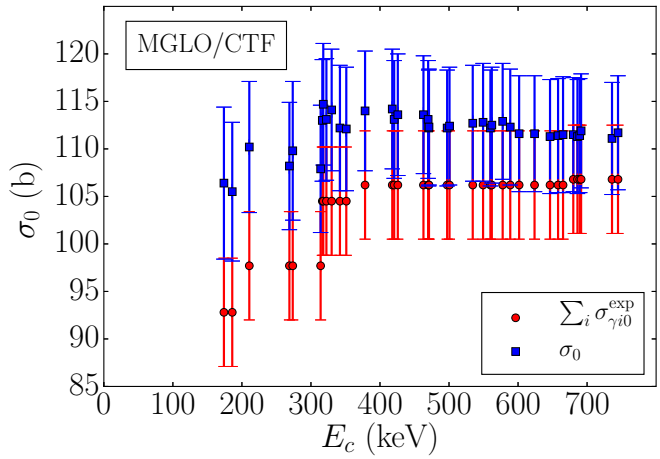

FIG. 9. Plot of the variation in the total radiative-capture cross section σ_0 and the sum of the experimental cross sections $\sum_i \sigma_{\gamma i0}^{\exp}$ for feeding the ground state as a function of the critical energy E_c, assuming the MGLO/CTF combination of PSF/LD models with an enhancement factor of $k_0 = 2.9$ and the LD parametrization from Ref. [40].

C. Neutron-separation energy for ^{186}Re

The primary γ rays listed in Table IV, a subset of which is shown in Fig. 1, were used to determine the neutron separation energy S_n for ^{186}Re by applying a global least-squares fit to the level energies from Refs. [10,55], including a correction for nuclear recoil. The resulting value for the neutron separation energy is $S_n = 6179.59(5)$ keV. This value is reasonably consistent with the adopted value $S_n = 6179.35(18)$ keV from the 2012 atomic mass evaluation (AME) [63], but the uncertainty on the value measured in this work is significantly smaller than the adopted value. The least-squares fit also produced smaller uncertainties in the excitation energies of known levels, listed in Table IV, than those reported in the adopted level scheme [10].

V. CONCLUSIONS

Past measurements of the total radiative thermal-neutron capture cross section for ^{185}Re have primarily been performed using neutron activation techniques. The neutron activation method requires precise knowledge of the neutron flux incident on the target, and determination of the cross section typically involves corrections for fast and epithermal contributions to the flux. In this work, we used the PGAA technique to measure γ-ray production cross sections for the ^{185}Re(n,γ) reaction, standardized using known ^{35}Cl(n,γ) cross sections from measurements with a stoichiometric $^{\text{nat}}$ReCl$_3$ target. The measured partial cross sections were combined with statistical-decay modeling to calculate a total radiative thermal-neutron capture cross section of $\sigma_0 = 111(6)$ b for ^{185}Re(n,γ), which independently confirms the results of earlier measurements made using activation and pile oscillator techniques. The existing literature values for σ_0 are compared with the measurement from this work in Table VII.

Spectroscopic analysis of the experimental prompt γ-ray data resulted in the discovery of 50 newly observed primary γ rays, which were combined with literature values for discrete-level energies in ^{186}Re to arrive at a new measurement of 6179.59(5) keV for the neutron separation energy in ^{186}Re. The independent measurement from this work, which has a smaller uncertainty than the adopted value from the 2012 AME [63], provides a useful input to future atomic mass evaluations.

Comparison of the modeled population, calculated using the DICEBOX code, with the experimentally-measured depopulation for individual levels is a powerful tool for evaluating the accuracy and completeness of nuclear-structure information. The results presented in this work include proposed adjustments to seven level J^π assignments and confirmation of all other tentative J^π assignments in the ^{186}Re level scheme [10] below an excitation energy of 746 keV. These results, combined with reduced uncertainties in level energies resulting from the global least-squares fit to the γ-ray and level energies, represent significant improvements to the ^{186}Re level scheme.

ACKNOWLEDGMENTS

This work was initiated under Defense Threat Reduction Agency Grant No. HDTRA1-08-1-0014 (YSU). Later work was performed under the auspices of the University of California, supported by the Director, Office of Science, Office of Basic Energy Sciences, of the US Department of Energy at the Lawrence Berkeley National Laboratory under Contract No. DE-AC02-05CH11231, and at Lawrence Livermore National Laboratory under Contract No. DE-AC52-07NA27344. Additional funding was provided by the Domestic Nuclear Detection Office of the Department of Homeland Security. Access to the Budapest PGAA facility was financially supported by the NAP VENEUS08 grant under Contract No. OMFB-00184/2006. This work was also supported by the Czech Science Foundation under Grant No. 13-07117S. The authors gratefully acknowledge the support of the operations staff at the Budapest Research Reactor. D.M. thanks Dr. C. J. Chiara for help reviewing the manuscript.

[1] R. B. Firestone, *Database of Prompt Gamma Rays from Slow Neutron Capture for Elemental Analysis*, (International Atomic Energy Agency, Vienna, 2006), https://www-nds.iaea.org/pgaa/egaf.html.
[2] Z. Révay, Anal. Chem. **81**, 6851 (2009).
[3] A. M. Hurst, R. B. Firestone, B. W. Sleaford, N. C. Summers, Z. Révay, L. Szentmiklósi, M. S. Basunia, T. Belgya, J. E. Escher, and M. Krtička, Phys. Rev. C **89**, 014606 (2014).
[4] M. Krtička, R. B. Firestone, D. P. McNabb, B. Sleaford, U. Agvaanluvsan, T. Belgya, and Z. S. Révay, Phys. Rev. C **77**, 054615 (2008).
[5] R. B. Firestone, M. Krtička, Z. Révay, L. Szentmiklósi, and T. Belgya, Phys. Rev. C **87**, 024605 (2013).
[6] H. D. Choi *et al.*, Nucl. Sci. Eng. **177**, 219 (2014).
[7] A. M. Hurst, R. B. Firestone, L. Szentmiklósi, B. W. Sleaford, M. S. Basunia, T. Belgya, J. E. Escher, M. Krtička, Z. Révay, and N. C. Summers, Phys. Rev. C **92**, 034615 (2015).
[8] C. Genreith, *Partial neutron capture cross sections of actinides using cold neutron prompt gamma activation analysis*, FZJ-2015-02574 (Nukleare Entsorgung und Reaktorsicherheit, 2015).
[9] M. Rossbach *et al.*, J. Radioanal. Nucl. Chem. **304**, 1359 (2015).
[10] C. M. Baglin, Nucl. Data Sheets **99**, 1 (2003).
[11] G. Schoeneich, H. Palmedo, C. Dierke-dzierzon, S. C. Mutter, and H. J. Biersack, Scand. J. Urology Nephrology **31**, 445 (1997).
[12] F. F. Knapp *et al.*, Appl. Radiat. Isotopes **49**, 309 (1998).
[13] L. Bernstein, D. Brown, A. Hurst, J. Kelly, F. Kondev, E. McCutchan, C. Nesaraja, R. Slaybaugh, and A. Sonzogni, Tech. Rep. LLNL-CONF-676585, Lawrence Livermore National Laboratory, Berkeley, California (2015).
[14] Evaluated Nuclear Structure Data File (ENSDF), Brookhaven National Laboratory, http://www.nndc.bnl.gov/ensdf/.
[15] R. Capote *et al.*, Nucl. Data Sheets **110**, 3107 (2009), https://www-nds.iaea.org/RIPL-3/.
[16] M. B. Chadwick *et al.*, Nucl. Data Sheets **112**, 2887 (2011), http://www.nndc.bnl.gov/exfor/endf00.jsp.
[17] R. M. Lindstrom and Z. Révay, in *Handbook of Prompt Gamma Activation Analysis*, edited by G. L. Molnár (Kluwer Academic, Dordrecht, 2004), Chap. Beams and Facilities, p. 31.
[18] L. Szentmiklósi, T. Belgya, Z. Révay, and Z. Kis, J. Radioanal. Nucl. Chem. **286**, 501 (2010).
[19] T. Belgya, Z. Kis, and L. Szentmiklósi, Nucl. Data Sheets **119**, 419 (2014).
[20] T. Belgya, in *JRC Scientific and Technical Reports: EFNUDAT Fast Neutrons*, edited by F. J. Hambsch (Publications Office of the European Union, Luxembourg, 2009), pp. 21–26.
[21] Z. Révay, T. Belgya, and G. L. Molnár, J. Radioanal. Nucl. Chem. **265**, 261 (2005).
[22] G. L. Molnár, Z. Révay, and T. Belgya, Nucl. Instrum. Methods Phys. Res. A **489**, 140 (2002).
[23] HYPERMET-PC version 5.01 (v512), Institute of Isotopes, Budapest, http://www.iki.kfki.hu/nuclear/hypc/.
[24] R. B. Firestone, C. M. Baglin, and S. Y. F. Chu, *Table of Isotopes: 1999 Update*, 8th ed. (Wiley-VCH, Weinheim, Germany, 1999).
[25] G. L. Molnár, Z. Révay, and T. Belgya, Nucl. Instrum. Methods Phys. Res. B **213**, 32 (2004).
[26] Z. Révay, R. B. Firestone, T. Belgya, and G. L. Molnár, in *Handbook of Prompt Gamma Activation Analysis*, edited by G. L. Molnár (Kluwer Academic, Dordrecht, 2004), Chap. Prompt Gamma-Ray Spectrum Catalog, p. 173.
[27] Z. Révay and G. L. Molnár, Radiochim. Acta **91**, 361 (2003).
[28] M. Berglund and M. E. Wieser, Pure Appl. Chem. **83**, 307 (2011).
[29] A. M. Hurst, N. C. Summers, L. Szentmiklósi, R. B. Firestone, M. S. Basunia, J. E. Escher, and B. W. Sleaford, Nucl. Instrum. Methods Phys. Res. B **362**, 38 (2015).
[30] R. Nowotny, XMUDAT: Photon attenuation data on PC, version 1.0.1, https://www-nds.iaea.org/publications/iaea-nds/iaea-nds-0195.htm.

[31] J. Beringer *et al.* (Particle Data Group), Phys. Rev. D **86**, 010001 (2012), G. Cowan, Statistics, p. 390.
[32] F. Bečvář, Nucl. Instrum. Methods Phys. Res. A **417**, 434 (1998).
[33] N. Bohr, Nature **137**, 344 (1936).
[34] C. E. Porter and R. G. Thomas, Phys. Rev. **104**, 483 (1956).
[35] S. F. Mughabghab, *Atlas of Neutron Resonances: Resonance Parameters and Thermal Cross Sections,* $Z = 1 - 100$, 5th ed. (Elsevier Science, New York, 2006).
[36] T. Kibédi, T. Burrows, M. Trzhaskovskaya, P. Davidson, and C. Nestor, BRICC v2.3S conversion coefficient calculator (2011), http://bricc.anu.edu.au/.
[37] T. Kibédi, T. W. Burrows, M. Trzhaskovskaya, P. Davidson, and C. Nestor, Nucl. Instrum. Methods Phys. Res. A **589**, 202 (2008).
[38] A. Gilbert and G. W. Cameron, Can. J. Phys. **43**, 1446 (1965).
[39] T. D. Newton, Can. J. Phys. **34**, 804 (1956).
[40] T. von Egidy and D. Bucurescu, Phys. Rev. C **72**, 044311 (2005).
[41] T. von Egidy and D. Bucurescu, Phys. Rev. C **80**, 054310 (2009).
[42] S. I. Al-Quraishi, S. M. Grimes, T. N. Massey, and D. A. Resler, Phys. Rev. C **67**, 015803 (2003).
[43] D. M. Brink, Ph.D. thesis, University of Oxford (1955).
[44] P. Axel, Phys. Rev. **126**, 671 (1962).
[45] S. G. Kadmenski, V. P. Markushev, and V. I. Furman, Sov. J. Nucl. Phys. **37**, 165 (1983).
[46] J. Kopecky and M. Uhl, Phys. Rev. C **41**, 1941 (1990).
[47] J. Kroll *et al.*, Phys. Rev. C **88**, 034317 (2013).
[48] A. M. Goryachev, G. N. Zalesnyi, S. F. Semenko, and B. A. Tulupov, Sov. J. Nucl. Phys. **17**, 236 (1973).
[49] S. S. Dietrich and B. L. Berman, At. Data Nucl. Data Tables **38**, 199 (1988).
[50] J. Kopecky, *Handbook for calculations of nuclear reaction data* (IAEA, Vienna, Austria, 1998), IAEA-TECDOC-1034, p. 97.
[51] J. Kopecky, M. Uhl, and R. E. Chrien, Phys. Rev. C **47**, 312 (1993).
[52] A. Richter, Nucl. Phys. A **507**, 99 (1990).
[53] J. Speth and A. van der Woude, Rep. Prog. Phys. **44**, 719 (1981).
[54] W. V. Prestwich, M. A. Islam, and T. J. Kennett, Z. Phys. A **315**, 103 (1984).
[55] C. Wheldon *et al.*, J. Phys. G **36**, 095102 (2009).
[56] D. A. Matters, N. Fotiades, J. J. Carroll, C. J. Chiara, J. W. McClory, T. Kawano, R. O. Nelson, and M. Devlin, Phys. Rev. C **92**, 054304 (2015).
[57] D. W. Seegmiller, M. Lindner, and R. A. Meyer, Nucl. Phys. A **185**, 94 (1972).
[58] R. G. Lanier *et al.*, Phys. Rev. **178**, 1919 (1969).
[59] J. Glatz, Z. Phys. **265**, 335 (1973).
[60] F. Bečvář, Y. Honzatko, M. Králík, N. D. Nhuan, T. Stadnikov, and S. A. Telezhnikov, Sov. J. Nucl. Phys. **37**, 809 (1983).
[61] S. C. Wu, Nucl. Data Sheets **106**, 619 (2005).
[62] T. Hayakawa, T. Shizuma, T. Kajino, S. Chiba, N. Shinohara, T. Nakagawa, and T. Arima, Astrophys. J. **628**, 533 (2005).
[63] M. Wang, G. Audi, A. H. Wapstra, F. G. Kondev, M. MacCormick, X. Xu, and B. Pfeiffer, Chin. Phys. C **36**, 1603 (2012).
[64] L. Seren, H. N. Freidlander, and S. H. Turkel, Phys. Rev. **72**, 888 (1947).
[65] H. Pomerance, Phys. Rev. **88**, 412 (1952).
[66] W. S. Lyon, Nucl. Sci. Eng. **8**, 378 (1960).
[67] R. A. Karam, T. F. Parkinson, and W. H. Ellis, Technical Report No. AD0402668, University of Florida, Gainesville, FL (1963), http://www.dtic.mil/docs/citations/AD0402668.
[68] S. J. Friesenhahn, D. A. Gibbs, E. Haddad, F. H. Fröhner, and W. M. Lopez, J. Nucl. Energy **22**, 191 (1968).
[69] R. E. Heft, Technical Report No. UCRL-80286, Lawrence Livermore National Laboratory (1980).
[70] F. De Corte and A. Simonits, At. Data Nucl. Data Tables **85**, 47 (2003).
[71] F. Farina Arboccò, P. Vermaercke, K. Smits, L. Sneyers, and K. Strijckmans, J. Radioanal. Nucl. Chem. **296**, 931 (2013).